TÉCNICO LISBOA

UNIVERSITÀ DEGLI STUDI DI PADOVA

Aging Impact of Permanent Magnets in Synchronous Machines for Traction Applications

Marco Spangaro

Thesis to obtain the Master of Science Degree in

Mechatronics Engineering

Supervisor(s): Prof. Fabio Tinazzi
Prof. João Filipe Pereira Fernandes

Per mio papà Giuseppe, che mi ha insegnato con i fatti cosa significhino la passione e la dedizione. Sei semplicemente il mio esempio.

Per mia mamma Fabiana, che più di tutti mi ascolta, mi capisce e mi aiuta. A parole non potrò mai descrivere la mia gratitudine.

Per mio fratello Luca, che mi ha preceduto nella carriera da Ingegnere. Il fatto che tu sia così forte in ciò che fai mi ha sempre messo paura, ma è grazie a questo stimolo che sono riuscito a arrivare qui ora.

Per mia sorella Alessandra, che è stata la motivazione per la quale ho intrapreso questa esperienza all'estero. Probabilmente senza i tuoi consigli non avrei mai vissuto i due anni più belli della mia vita.

Per Nonna Fiorina ma anche per chi non c'è più. Nonno Tony e Nonna Ghita, mi sarebbe piaciuto avervi con me per festeggiare questo traguardo.

Declaration

I declare that this document is an original work of my own authorship and that it fulfills all the requirements of the Code of Conduct and Good Practices of the Universidade de Lisboa.

Acknowledgments

I would like to say a few words to thank the people who helped me during this experience at Instituto Superior Técnico.

First of all, the biggest thank you goes to my family, who has always supported me during these years. You never made me feel any kind of pressure and at the same time you helped me to always stay focused on the goal.

Secondly, I would like to especially thank my supervisor, Prof. Joao Fernandes, for his availability and incredible patience during these months of thesis. When I started this work I felt lost but thanks to him I always felt comfortable to ask questions. At the same time I have always been stimulated by our meetings to learn more and to search for the best way to do my task. This is a lesson that I am sure I will carry with me throughout my professional career.

I extend the same appreciation to my co-supervisor, Eng. Pedro Bhagubai. For always being helpful when I asked for help, encouraging me to ask for more without hesitation. His help from a technical point of view was invaluable, but more than anything else I can say that I was lucky to meet the person, even before the engineer.

I certainly can't forget all the people in the Electrical Machinery lab. Here I found a great team and a sparkling environment that stimulated me to grow. In particular I would like to thank Eng. Luis Bucho, Eng. Francisco Silva and Eng. Joao Reves for their interest in helping me in my work and their sympathy. During these months I spent many hours in the lab. and it is also because of your presence that I was able to work with pleasure and motivation.

Finally, thanks to all the colleagues with whom I have shared something over the years, both at the University of Padua and at the Instituto Superior Técnico. You have enriched me as a person and I could not be more grateful for what I have experienced with you over these six years.

Abstract

With the continuous electrification of the industrial and transportation systems, higher demanding specifications are being imposed on electrical motors, leading to higher degradation due to the aging of their components.

This thesis focuses its attention on the study of the effect that the degradation of the magnetic properties of permanent magnets, as a result of exposure to elevated temperatures, has on the performance of the electrical machines in which they are applied.

A comprehensive study was conducted, comprising an experimental part in which the magnets were subjected to aging following exposure to high temperatures and a simulative part in which the data obtained was used for finite element analysis to define how the decay of magnetic properties affects a synchronous motor performance. Initially, a method for measuring magnetic flux density was designed, implemented, and validated. This exploits the induction law to obtain the average value of flux produced by permanent magnets from a voltage measurement. After that, aging tests at 140℃ till 186 hours were performed on three samples of NdFeB magnets to observe changes in their magnetic properties, particularly the decay of magnetic flux density. The measurements showed no appreciable decay, so a fourth sample of another magnet grade was tested but again no aging was found. For this reason, it was decided to consider previously obtained data from a previous master thesis to develop the simulation part. The experimental results were integrated by a detailed finite element analysis to simulate the impact of the observed degradations on machine performance in terms of torque generation and efficiency.

The results of the aging tests on the permanent magnets show a decrease in magnetic flux density for prolonged periods. This is reflected in the torque produced by the motor in a negative way. In addition, effects, albeit marginal, were found on machine efficiency.

However, as explained above, it will be vital to carry out further aging tests in the future to understand how magnets actually age.

Keywords: Aging, Permanent Magnet, Operating Point, Permanent Magnets Synchronous Motor, Finite Element Analysis

Contents

List of Tables

List of Figures

Nomenclature

Greek symbols

η	Efficiency
μ_0	Vacuum magnetic permeability
ω	Mechanical rotational speed
ψ	Linked magnetic flux
ρ	Electrical resistivity
σ	Standard deviation

Roman symbols

B	Magnetic flux density
f	Frequency
H	Magnetic field strenght
i	Current
J	Magnetic polarization
M	Magnetization
P	Losses
R	Electric resistance
T	Torque
u	Voltage

Subscripts

max	maximum value

Superscripts

$\langle a \rangle$	Average value
$\|a\|$	Absolute value

Acronyms

FEA	Finite Element Analysis
FeSi	Silicon-Iron
IPMSM	Internal Permanent Magnet Synchronous Motor
NdFeB	Neodymium-Iron-Boron
PC	Permeance Coefficient
PM	Permanent Magnet
PMSM	Permanent Magnets Synchronous Motor

Chapter 1

Introduction

1.1 Motivation

The increasing use of electrical machines in applications where high specific power and high efficiency are required has led to the need to study the effects of stress on materials over long periods of time. These types of machines usually have high operating temperatures [1–3], which can cause premature aging of materials, i.e. loss of performance as a result of changes in physical and chemical structure. Such aging can adversely affect the performance of the machine even during its design life. In particular, it is typical to have, besides mechanical losses, also core losses, demagnetisation of Permanent Magnets (PMs) and degradation of winding insulation [2, 4–6]. There can be many causes: thermal, electrical and mechanical stresses over time are the most relevant.

Increasing the specific power of the machine and reducing material aging can be a daunting challenge as these two concepts are in opposition to each other in practice. In fact, increasing specific power leads to increasing degradation rates. This is caused by the fact that the machine is subjected to ever-increasing electromechanical and thermal loads. Optimal electrical machine design, optimization tools combined with finite element analysis (FEA) and aging prediction models can be used to maximise specific power and efficiency and mitigate material degradation [4, 7]. In the past, models have been created to understand the effects of aging on Neodymium-Iron-Boron (NdFeB) PMs, Silicon-Iron (FeSi) laminated cores and electrical insulations. In [8], an experimental study on the effects of PM aging was conducted to evaluate its possible impact on Permanent Magnet Synchronous Motors (PMSMs), motors widely used in industry. Other studies have focused more on the consequences of aging in the FeSi core, as in [9]. Aging prediction is typically based on the Arrhenius aging method [10].

In electrical machines with high specific power, materials are usually tested in order to extend their current limits so as to achieve higher performance in terms of generated torque, speed etc. In these limit cases, the effects of aging are likely to have a more pronounced impact than in solutions where high specific power is not required.

1.2 Objectives

The thesis work will focus on the impact of aging PMs in synchronous machines for traction applications. To achieve a proper understanding and study of the PM aging in synchronous machines, the following methodology is proposed:

- Development of a reliable, cheap and fast method for measuring the PMs magnetic flux.
- Experimental aging of PMs under different magnetic and thermal operational points.
- Modelling of the aging effects using the Arrhenius model.
- Study of the performance of a synchronous motor for different stages of aging.

Chapter 2

Background

The aim of this chapter is, after a review of the most important concepts concerning the Permanent Magnets (PMs), to provide an introduction to the effect of aging on Neodymium-Iron-Boron (NdFeB) PMs, finally focusing on the consequences of this aging on the performance of Permanent Magnet Synchronous Motors (PMSMs).

Through a critical review of the literature and available technologies, the current landscape of magnetic measurements will be outlined, identifying the most significant advances and the gaps that still persist in the field. This chapter will provide a solid foundation to contextualise the research I carried out and is preparatory for the reader to follow each step of the thesis in detail.

2.1 Permanent Magnets applications

PMs find applications in a wide range of sectors, owing to their remarkable magnetic properties and their ability to provide a reliable source of magnetic energy in various devices and systems. In the automotive industry, which is the case related to this project, they are inserted in electric vehicle motors, enhancing efficiency and reducing emissions [11–13]. Renewable energy sectors, such as wind power [14, 15] and hydropower [16], rely on PMs for efficient electricity generation. Beyond these, the aerospace industry [17, 18], consumer electronics, manufacturing, and even the defense sector [19] utilize PMs for their compact, lightweight, and enduring magnetic properties, making them an essential and irreplaceable component in the modern world of technology and innovation.

When it comes to PMs, one of the most widely used and highly regarded materials, as shown in Figure (2.1), is NdFeB. This material has gained popularity in a multitude of applications due to its exceptional properties: NdFeB magnets offer a compelling combination of high magnetic strength, energy density, cost-efficiency, and versatility [20–22]. For the thesis, this very material was used for the study.

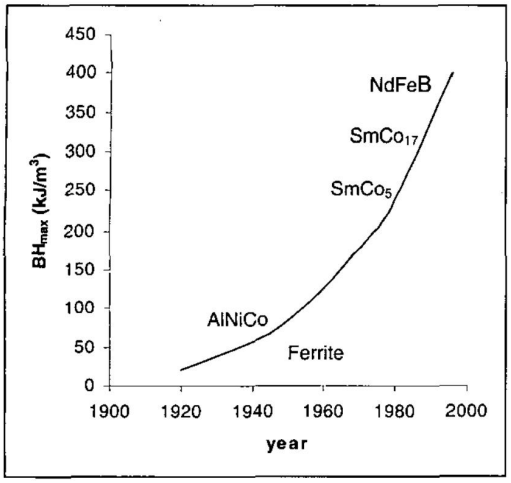

Figure 2.1: Permanent Magnet materials developement [20]

So far, the main applications of PMs in industry have been explained. Now it is time to place their use in the world of traction by giving an overview of the main types of electric motors used in this sector. The world of electric machines is very wide and constantly growing and in the specific case of traction applications there are different kinds of motors available in the market today. The selection of any specific motor for the electric propulsion system depends on various factors such as its simple structure, lightweight, small volume, low cost, easy and flexible electric drive control, fault tolerance capability, low acoustic noise level, better starting torque feature, high efficiency and high power density, constant torque and constant power regions over a wide speed range, fast and quick torque response and operational reliability on different driving conditions [23].

According to [23–25], the development of power electronics has resulted in three-phase induction and PM machines being the most commonly used in the electric and hybrid electric vehicles, as shown in Figure 2.2.

Make	Model	Traction Motor
Honda	EV Plus	DC Motor
Holden	Ecommodore	SRM
Nissan	Tino,Leaf,Altra	PMSM
Honda	Insight,Accord,Civic	PMSM
Toyota	Prius C & V	PMSM
Toyota	Highlander,Avalon	PMSM
Toyota	Camry	PMSM
Ford	Fusion SE Hybrid	PMSM
Ford	C Max Hybrid SEL	PMSM
Hyundai	Blueon	PMSM
Chevrolet	Volt & Energi	PMSM
Renault	Kangoo	IM
Chevrolet	Silverado	IM
Daimler Chrysler	Durango	IM
Tesla	Roadster	IM
Honda	Fit EV	IM
Toyota	Reva4	IM
REVA	NXR	IM
Ford	Focus Electric	IM
Ford	Transit Connect	IM
GM	EV1	IM
BMW	X5	IM

Figure 2.2: Electric motors for traction applications [23]

As far as the full electrial and hybrid worlds are concerned, to date almost the entire light vehicle sector has switched to PMs to meet power density and efficiency requirements (see Figure 2.3), in particular IPM is becoming the dominant type of machine [24]. On the other hand, referring to the medium-heavy vehicle category (e.g. delivery trucks or buses), the authors in [24] point to the induction motor as the main protagonist, while noting an increased interest in IPM. As far as the rail sector is concerned, once again the induction motor is the main player. However, more recently, PM motors have been developed for high-speed rail [24]. To conclude their article, in [24], the authors predict that in the near future, PM machines will continue to dominate the light-duty vehicle market and expand more in the medium/heavy-duty industry and high-speed rail applications.

Motor characteristics	DC	IM	PMSM	SRM
Power density	2.5	4	5	3.5
Efficiency	2.5	4	5	4.5
Controllability	5	5	4	3
Reliability	3	5	4	5
Robustness	3	5	4	5
Torque density	3	4	5	4
Speed range	2.5	4	4.5	4.5
Required maintenance	3	4	4	4
Torque ripple/noise	3.5	4.5	4.5	3
Over load capability	3	4	4	4
Technical maturity	5	4.5	4	3.5
Life time	3.5	5	4	4.5
Size and weight	3	4	5	4
Cost	4	5	3	4
Total	46.5	62	60	56.5

Figure 2.3: Evaluation of electric motors [23]

2.2 Permanent Magnets characteristics

The first thing to analyse in the field of PMs is the BH curve, an example of which is shown in Figure 2.4. It is also known as the magnetization curve or hysteresis loop and it is a critical concept in the realm of magnetic materials, such as the PMs. It graphically represents the relationship between magnetic field strength (H) and the magnetic induction or flux density (B) in a material [5, 20]. This curve provides essential insights into how magnetic materials respond to external magnetic influences. The significance of the BH curve for PMs lies in its ability to depict the magnetic behavior of these materials under various conditions, such as magnetization, demagnetization, and exposure to external fields.

Understanding the BH curve is pivotal for PMs because it helps in characterizing their performance, such as their coercivity (ability to resist demagnetization) and remanence (the residual magnetization when the external field is removed). This knowledge is indispensable for designing efficient magnetic systems and optimizing the use of PMs in applications like electric motors, generators, and medical devices. By tailoring the magnetic properties to specific requirements, it is possible to ensure that PMs operate reliably and efficiently, making the BH curve a cornerstone in the development of these critical components in modern technology.

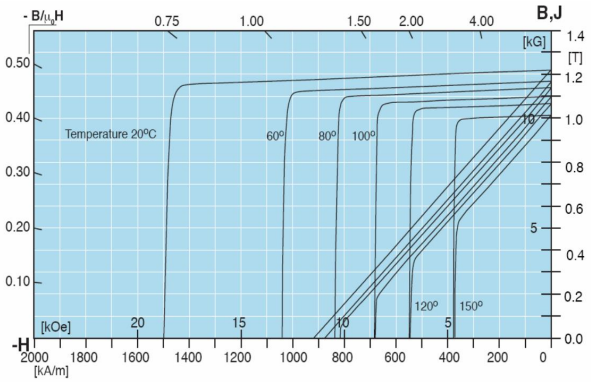

Figure 2.4: Demagnetization curves [22]

Another important feature to be analysed are the so-called operating points. The operating point of a PM refers to the magnetic state at which the magnet operates under specific conditions. It is characterized by a combination of parameters, including the magnetic field strength and magnetic induction. The operating point is significant because it helps determine the magnet's performance, particularly its ability to provide a stable and strong magnetic field. Understanding and controlling the operating point is crucial in various applications, such as electric motors, generators, and sensors, where the magnet must function within a defined range to meet desired specifications. The choice of operating point can impact efficiency, hysteresis losses, and demagnetization risks, making it an essential consideration in the design and application of PMs [26].

Determining the operating point of a PM involves the intersection of its load line with the demagnetization curve. The specific position of this intersection is influenced by the conditions to which the magnet is subjected, whether it is operating in an open circuit or as part of a specific magnetic circuit (which will be the case of this study). The load line's steepness can be computed using Equation 2.1 as it is easy to understand looking at Figure 2.5 and is commonly known as the Permeance Coefficient (PC) [5, 27, 28]. This PC is a vital parameter in PM analysis, providing insight into the magnet's behavior under different scenarios and configurations, helping understand and optimize magnetic performance.

$$PC = -\frac{B_m}{\mu_0 H_m} \tag{2.1}$$

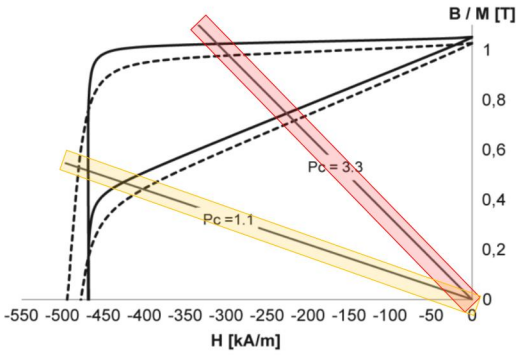

Figure 2.5: Load line (PC) highlighting, adapted [29]

2.3 Permanent Magnet flux density measurements

As stated in [30], the characterisation of PMs can be carried out in two distinct ways: in an open or closed magnetic circuit. The difference is that in the former the PM is not in contact with any ferrous parts, whereas in the latter case it is in direct contact with magnetic parts. Nowadays, there are several international and national standards recommending methods for measuring the magnetic properties of materials in a closed circuit [30], which will also be the case of this work.

As introduced in Section 1.2, the initial part of the thesis will focus on defining a reliable, fast and cheap method for obtaining precise measurements of the magnetic flux density of the PMs to be tested.

Measuring the magnetic flux of PMs can be achieved through several methods [30, 31], each with its own set of advantages and disadvantages in terms of precision, cost and time required to take measurements.

It is possible to divide the methods for direct measuring B into two families: free magnets or assembled systems [30]. With regard to the former, demagnetisation curves can be determined using the hysteresis graph, pulsed field magnetometer or Foner magnetometer (VSM). In the case of assembled systems, it is possible to use Gaussometer, or alternatively Hall probe. They are both instruments able to give real-time measurements and that can provide high sensibility. Figure 2.6 shows and highlights these methods, also comparing the level of accuracy.

	Measuring method	Parameters	Units	Equipment	Accuracy (%)
	Measuring of free magnets				
1	Demagnetization curves	J(H), B(H)	T, kA/m	Hysteresis graph	(+/-) 1
2				Puls field magnetometer	(+/-) 1
3				Foner magnetometer (VSM)	(+/-) 0.5
4	Remanence in open circuit	JoC	T	Helmholtz Coil	(+/-) 1
5	Magnetic moment	Mm	Vs cm	Helmholtz Coil	(+/-) 1
6	Angel deviations	J	grad	Helmholtz Coil	(+/-) 0.5°
7				3 D mapper	(+/-) 0.5°
8	H(B) in a test point	B	T	Gauss meter/ Hall probe	(+/-) 1
9				3 D mapper	(+/-) 1
10	Surrounding coil	Φ	Vs cm	Coil and fluxmeter	(+/-) 0.5
11	Holding force	Φ	N	Dynamometer	2 - 5
	Measuring of assembled systems, for example rotors				
12	H(B) in the air gap	B	T	Gaussmeter / Hall probe	1 - 2
13	EMF	Ueff	V	Motor coil / Voltmeter	1

Figure 2.6: Methods to measure magnetic flux in PM [30] adapted

For reasons that will be explained in Chapter 3 it was decided to adopt a different method which is based on the induction law and allows to define the magnetic flux of the PM without a direct measurement of its magnitude. This method is the search coil and offers non-invasive measurements by analysing the voltage pulse generated at the coil when it is hit by a varying magnetic field. Nonetheless, it is relatively less sensitive than the ones previously listed, so it needs particular attention when applied.

2.4 Temperature effects on Permanent Magnets

Temperature plays a significant role in the aging process of PMs. In fact, over time, exposure to elevated temperatures can accelerate the aging of PMs, which refers to the gradual deterioration of their magnetic properties [28, 29, 32]. This phenomenon is primarily due to the thermal energy at higher temperatures, which causes increased atomic and molecular motion within the magnet's microstructure, leading to domain disruptions and magnetic domain wall movements. As a result, the magnet's remanence and coercivity, which are critical magnetic characteristics, may degrade. The rate of aging is often exponential, meaning that even slight temperature increases can have a substantial impact on a magnet's longevity as shown in Figure 2.7. This Figure also proves how the PC influences the aging of PMs.

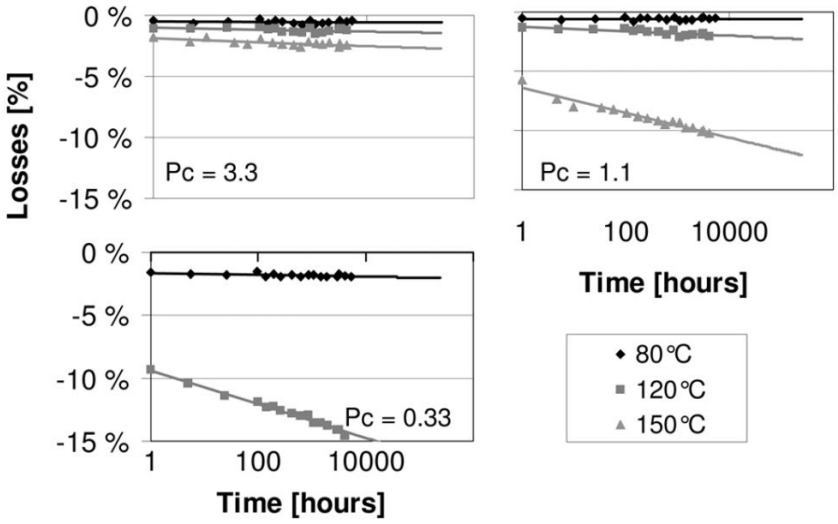

Figure 2.7: Losses as a function of time for different temperatures and PCs [32]

As just shown above and also introduced in Section 2.3, the magnetic circuit in which a PM is situated exerts a significant influence on the magnet, so much so that it also has a decisive impact on the thermal aging process. It influences the trajectory and dispersion of magnetic flux, potentially altering the magnet's effectiveness as time passes. In an ideal scenario, the magnetic circuit would maintain a closed-loop structure, ensuring that the magnetic field lines follow a well-defined path. However, in real-world applications, factors such as design, materials, and geometric constraints can lead to magnetic circuit irregularities. These irregularities can result in localized variations in magnetic field strength and may subject certain regions of the magnet to increased stresses or higher temperatures. Such conditions can accelerate aging processes like thermal demagnetization and lead to reduced magnet performance over time [28, 29, 32]. Proper design and optimization of the magnetic circuit are essential in preserving the long-term performance and reliability of PMs in various applications.

In [27, 28, 32], the aging experiments for PMs were conducted without these magnets being placed within a magnetic circuit. The value of the PC was solely determined by the physical dimensions of the magnets, specifically their height, length, and width. However, since the final objective of this thesis is to

assess the impact of aging PMs within a PMSM, the aging process will be carried out with the magnets inserted into a magnetic circuit. Another important motivation for this, is that in open circuit the PC is lower, which typically brings the PMs to more dangerous situations, close to the demagnetization knee.

In the study described in [33], the authors examined the magnetic behavior of PMs when subjected to various temperatures during aging, both with and without being situated in a magnetic circuit. They exposed samples of two different types of NdFeB magnets (as outlined in Table 2.1) to a range of temperatures for a minimum of 500 hours.

Table 2.1: Properties of tested materials in [33]

Material	Room temperature coercitivity H_c [kA/m]	Room temperature remenance B_r [T]	Temp. coeff. of B_r [%/°C]	Temp. coeff. of H_c [%/°C]
1	1730	1.25	-0.11	-0.64
2	1680	1.21	-0.09	-0.62

In the case of [33], the authors employed a different approach to determine the PC value when the PMs were not placed within a magnetic circuit. This method relied solely on the physical dimensions of the magnets and could be calculated using Equation 2.2 , where 'h' represents the height (in the direction of magnetization), 'l' denotes the length, and 'w' represents the width of the magnet [33].

$$PC = 1.77\frac{h}{lw}\sqrt{h(l+w)+lw} \tag{2.2}$$

In [33], for experiments involving PMs placed within a magnetic circuit, the researchers designed a magnetic setup consisting of a yoke made from laminated electrical steel. The PMs were situated at the center of this yoke, as depicted in Figure 2.8.

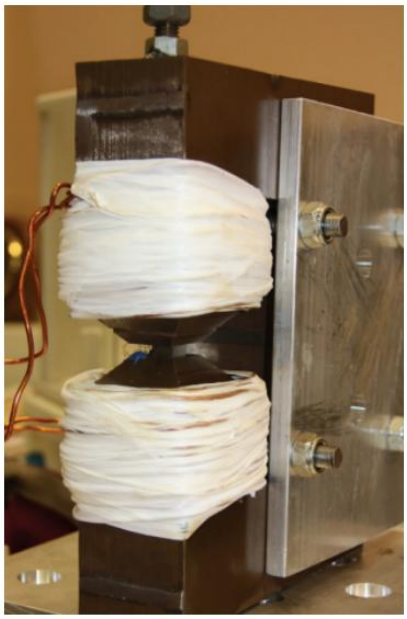

Figure 2.8: Iron yoke used to test the materials [33]

Additionally, two coils were wound around the yoke to generate an excess magnetic field reaching up to 560kA/m. This entire system was employed during the aging process. After cooling the system back to room temperature, they measured the magnetic flux using a Helmholtz coil and determined the magnetic field strength using a Hall sensor.

The results obtained from their aging experiments exhibit the same gradual decline in flux losses as introduced before. However, these results also featured a comparison of polarization losses for PMs aged inside a magnetic circuit (referred to as ”closed circuit exposure”) and PMs aged without being placed in a magnetic circuit (termed ”open circuit exposure”).

Despite the initial losses being relatively modest, when the PMs were positioned within the magnetic circuit, it was evident that the rate of time-dependent demagnetization experienced a significant decrease with the increase in field strength. In [33], the authors utilized the logarithmic law to predict how the polarization losses of the tested samples would evolve under the given conditions. Figure 2.9 presents the estimated polarization loss for durations of 1 hour and 30 years, with respect to the PC, at a temperature of 120℃. Notably, there is a distinct difference between the time-dependent losses for magnets not placed in a magnetic circuit and those inserted in magnetic circuits. Specifically, when PC = 1.0, the results for magnets within magnetic circuits show lower polarization losses. This indicates that, in reality, measurements in open circuit conditions provide more conservative estimates at PC = 1.

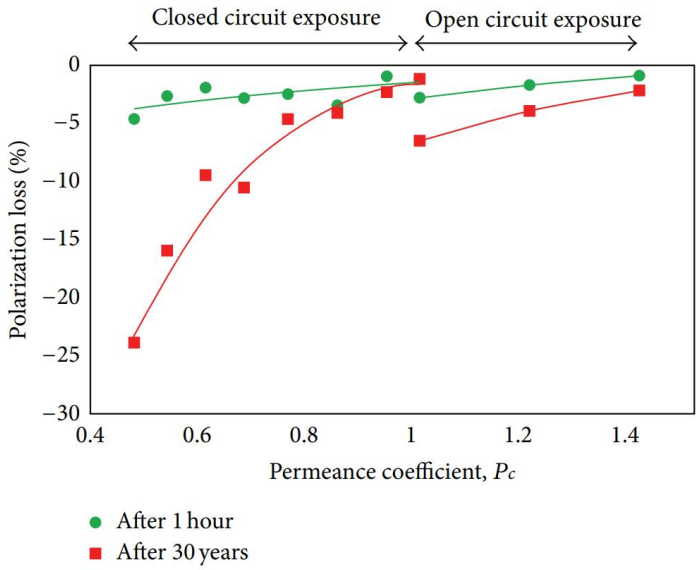

Figure 2.9: Estimated polarization losses as a function of PC in closed- and open-circuit exposures in material 2 magnets at 120° C [33]

The observed time-dependent polarization losses were found to be higher when the PMs were not positioned within a magnetic circuit. The authors in [33] suggest that this difference may be attributed to variations in the self-field during the initial demagnetization of open circuit magnets, which in turn affect their time-dependent behavior. Although this assertion lacks direct experimental validation, it underscores the idea that localized changes in field conditions for magnets not placed within a magnetic circuit can alter the PC value. For this reason, it appears more advantageous to have PMs inserted in a magnetic circuit to obtain results that align with the conditions within PMSMs.

2.5 Effects of Permanent Magnets aging on PMSMs

Since the ultimate goal of this thesis is to determine how thermal aging of PMs affects the performance of a PMSM, this section is dedicated to reviewing the state of the art on this topic.
As already introduced in Section 2.4, it is well known that exposure to high temperatures of a PM causes its performance to collapse. Anyway, to date there are not many studies about the effect that this aging has on PMSMs performance. Typically, during its operation, a PMSM can have a wide operating temperature range. For example, in [1], a wide temperature range PMSM is designed, which can be used as a servo mechanism of an electric actuator in a missile. In this case, the authors considered that the operation temperature can between -165℃ or -240℃.

In another study, [34], the authors considered a temperature range of 25℃ to 150℃ (6 simulations at steps of 25℃ each) for PMs applied in a PMSM and also analysed the effects on torque, speed and current. In terms of torque, they observed that the lowest temperature simulation had 18.52% more torque than the highest temperature simulation, as it is noticable in Figure 2.10. In terms of speed, it was seen that the magnet reached its steady-state speed faster at lower temperatures. In terms of current, it was found that the current in each phase rise as the temperature rise. These results are not directly related to aging, because short-term experiments are being dealt with, however, they can still be linked to the problem that this thesis wants to analyse.

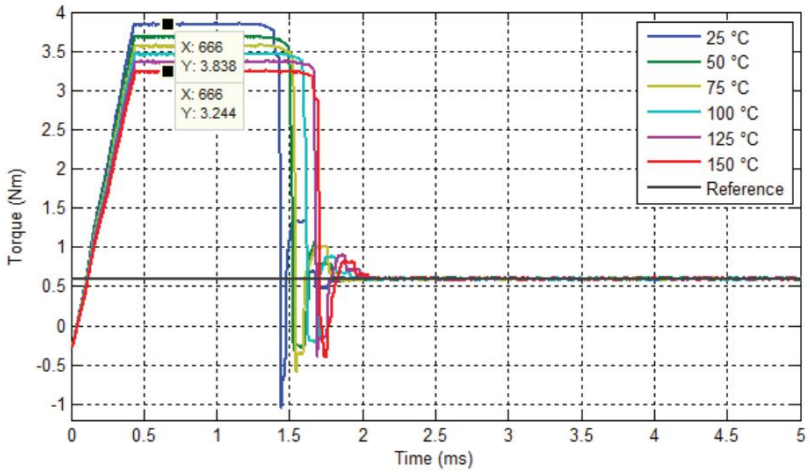

Figure 2.10: Torque-time curves obtained for all temperatures[34]

Chapter 3

Aging tests of Permanent Magnets

This chapter is dedicated to illustrating the methodology applied and the results obtained during the aging experiments. The chapter is composed of several sections in which the reader will be guided through the fundamental steps performed to define a reliable, fast and economical method to evaluate the thermal aging of NdFeB Permanent Magnets (PMs). Finally, once the method has been validated, the results obtained in the aging tests will be presented and discussed.

3.1 Equipment used

Three samples of a batch of grade BMN-42SH (Figure 3.1(a)) that were already present in the laboratory were used to test the NdFeB PMs. However, as will be discussed later, due to some unexpected results, a sample of grade BMN-48SH (Figure 3.1(b)) was used to evaluate the quality and reliability of the measurement method employed.

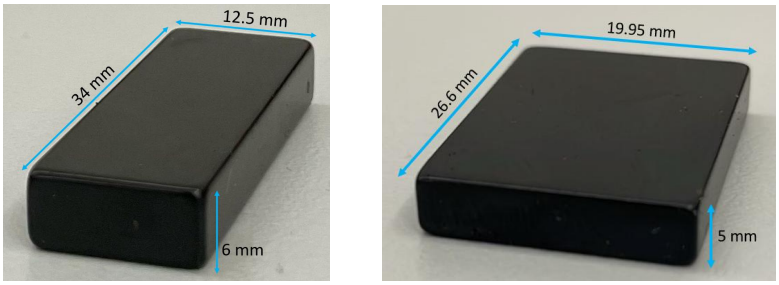

(a) BMN-42SH sample (b) BMN-48SH sample

Figure 3.1: Samples used

Table 3.1: Samples main characteristics

	BMN-42SH	BMN-48SH
B_r [T]	1.33	1.41
H_c [kA/m]	1018	1595
Crit. temp. [℃]	150	150

The main characteristics of the samples used are shown in Table 3.1, more information on this can be obtained from the datasheets in Appendices A and B. The magnets of Figure 3.1 were applied in the core consisting of laminated FeSi of Figure 3.2. This created a well-defined path for magnetic flux produced by the PMs.

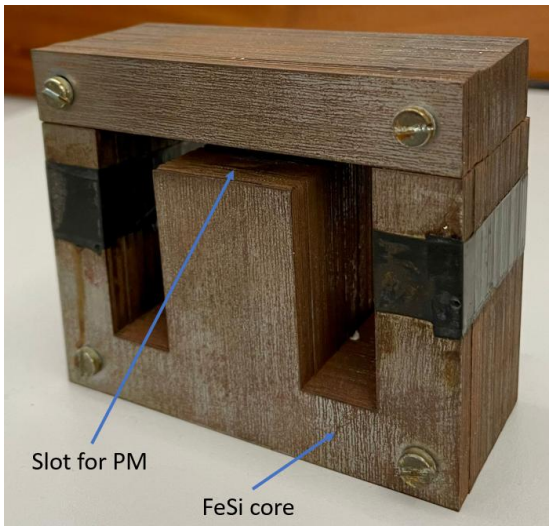

Figure 3.2: FeSi core to place the PMs

Three different operating points were considered when using the BMN-42SH samples and one operating point for the BMN-48SH sample. These depended on the thickness of the air gap that was artificially created between the bottom and top of the iron core by means of aluminium foil, as can be seen in Figure 3.3. The thicknesses used and their respective operating points are shown in Table 3.2, in which PMs have also been given a Code Name for ease of use in the following sections.

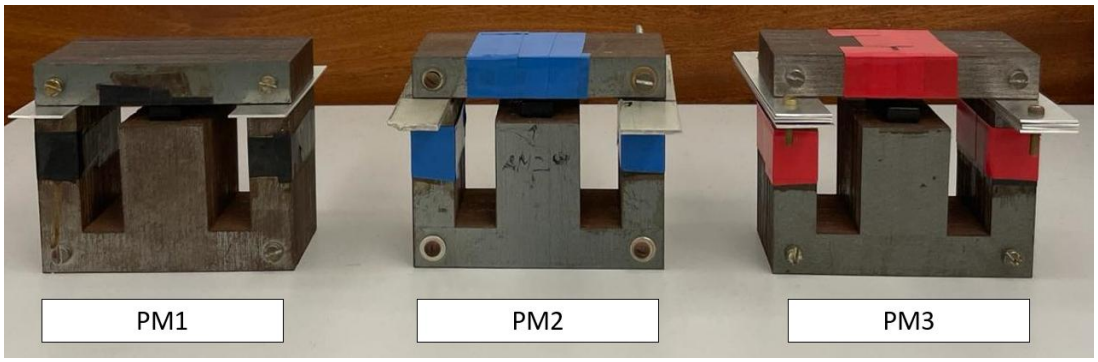

Figure 3.3: The three BMN-42SH magnets inserterd in the core, with different air gaps

Table 3.2: Relations between air gaps and PC

Code Name	Grade	Air gap [mm]	PC
PM1	BMN-42SH	1	≈ 4.5
PM2	BMN-42SH	2	≈ 2.3
PM3	BMN-42SH	4	≈ 1.1
PM4	BMN-48SH	2	≈ 2.3

3.2 Definition of the measurement method

In section 2.3, several methods have been introduced to define the magnetic flux (B_m) produced by PMs. The method used in this work is the so-called search coil method which exploits the induction law represented by Equation 3.2.

$$u(t) = Ri(t) - NS\frac{dB_m(t)}{dt} \tag{3.1}$$

Where R is the resistance of the coil, N is the number of turns of the coil, S is the cross sectional area and $\frac{dB_m(t)}{dt}$ is the variation of magnetic flux in time. Since no current is present in the coil so Equation 3.1 becomes Equation 3.2.

$$u(t) = -NS\frac{dB_m(t)}{dt} \tag{3.2}$$

Equation 3.2 shows that, if the coil is hit by a time-varying magnetic flux $B_m(t)$, a voltage pulse $u(t)$ will be generated. From $u(t)$, knowing the value of the constant product NS, it is possible to obtain the value of $B_m(t)$, as illustrated in Equation 3.3.

$$B_m(t) = -\frac{1}{NS}\int_0^\tau u(t)\,dt \tag{3.3}$$

Finally, considering the maximum value assumed by $B_m(t)$, one obtains the average value of the magnetic flux produced by the PM, indicated by $\langle B_m \rangle$.

As can be seen, the main criticism is that this is an indirect method: mathematical steps are required to derive $\langle B_m \rangle$ starting from a voltage measurement. This may make this method less accurate than others listed above, such as the direct use of a gaussmeter. However, this method was chosen for two main reasons: the speed of the measurement process and the fact that it returns $\langle B_m \rangle$. In fact, the PM could age non-homogeneously and if it is applied a 'spot' method (e.g. using a gaussmeter) one could achieve untruthful results that would compromise the correct aging analysis. The main stumbling block of this method is therefore being able to create a setup that guarantees a level of precision adequate for our purpose. The first step was to design the Printed Circuit Board (PCB) coil shown in Figure 3.4.

Figure 3.4: PCB coil used to perform the voltage measurements

This was designed through the use of Altium Designer. The critical issue at this stage was to evaluate and decide on the coil size, number of windings, and PCB size and thickness. All these design parameters are shown in Table 3.3.

Table 3.3: PCB parameters

PCB length	PCB width	PCB thickness	Max coil length	Max coil width	Number of turns
154 mm	65.9 mm	0.8 mm	34 mm	12.5 mm	8

The length and width of the PCB were designed in such a way that the PCB could slide perfectly between the top and bottom part of the FeSi core, over the PM. The thickness of 0.8 mm is crucial because it makes it possible to fit the coil between the top and bottom part of the core. In fact, the smallest possible air gap (1 mm) was always used during the measurements in order to obtain precise values. As can be seen in Figure 3.4, the coil extends in a horizontal direction, the perimeter having an area equal to that of the BMN-42SH PMs. Finally, based on the experiences of previous colleagues, it has been decided that a winding number of 8 was adequate to obtain a good voltage signal for analysis.

One end of the PCB was attached to a spring, the purpose of which was to ensure sliding in a horizontal direction, while the other end was connected to a voltage probe, which in turn was connected to the oscilloscope for displaying the voltage pulse, as shown in Figure 3.5.

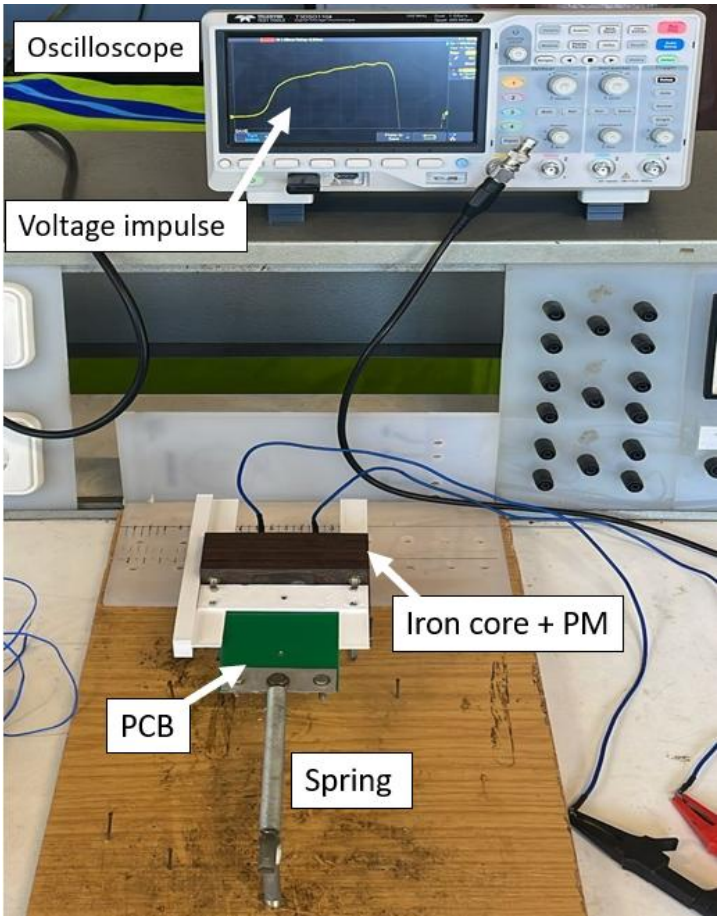

Figure 3.5: Illustration of the method applied

An important step before proceeding to the validation of the prepared setup which is not yet dealt with in detail is the definition of the constant parameter given by the product NS. In fact, looking at Equation 3.3, once the voltage pulse has been obtained, this is the only unknown in order to obtain the real value of $B_m(t)$.

The PM was removed from the magnetic circuit, then a coil with the characteristics of Table 3.4 was inserted into the central tooth of the ferromagnetic core and connected to a sinusoidal voltage source.

Table 3.4: Primary coil characteristics

Wire cross section	0.5 mm^2
Resistance	3.8 Ω
Number of turns	250

Above the primary coil, the secondary coil (the PCB coil) was placed and the magnetic circuit was closed again without any air gap placed in between. Between the secondary coil and the top of the ferromagnetic core, the gaussmeter was inserted to measure B, trying to place it in a central position with respect to the PCB coil section. In addition, the terminals of the secondary coil were connected to the oscilloscope to display the sinusoidal voltage induced u on it, the system just described is the one shown in Figure 3.6.

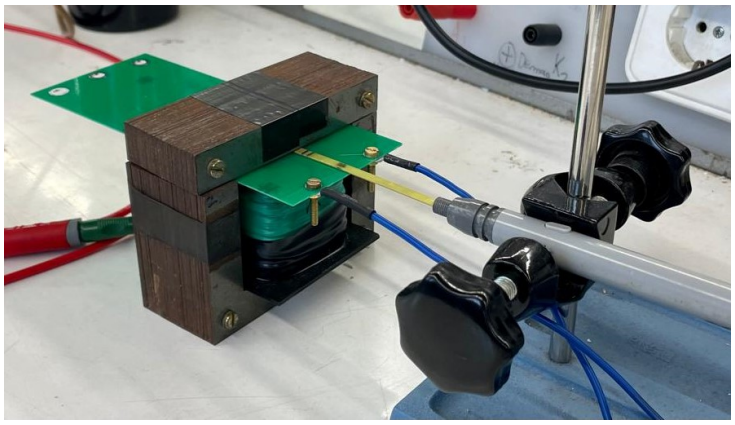

Figure 3.6: Setup to estimate NS of the PCB coil

To induce the sinusoidal voltage on the secondary coil, the primary coil was energized and an example of the waveforms obtained from the oscilloscope is the one shown in Figure 3.7. Now, having the waveforms of Figure 3.7 and starting from Equation 3.2, it is possible to derive NS as given in Equation 3.4.

$$NS = -\frac{\int u(t)\,dt}{B(t)} \tag{3.4}$$

This experiment was repeated for 27 different couples of values of supply voltage u and frequency f. After analysing the data obtained, the result was NS = 0.002516. This result comes from an average of the values obtained in the different experiments performed, however, it should be considered that, among the measurements performed, a percentage standard deviation $\sigma_{\%}$ = 1.1% was obtained, which

can be considered an acceptable value. Furthermore, it is important to remember that NS only comes into play as a constant parameter when one has to define $\langle B_m \rangle$, which means that even an inaccurate estimate would not influence the results recorded during the aging tests.

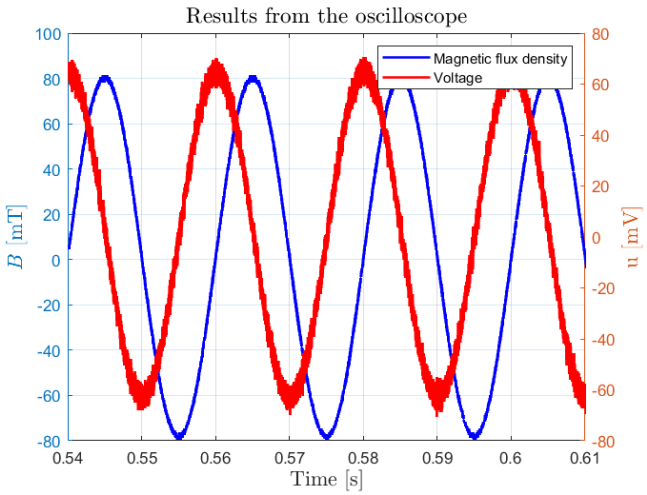

Figure 3.7: Waveforms obtained following the power supply of the primary coil

3.3 Validation of the measurement setup

As introduced in the previous section, the hurdle to overcome is to be able to construct a setup that allows for sufficiently precise measurements for the purpose. Indeed, it must be remembered that, the expected aging of PMs after around 200 hours ranges between 1% and 3%. Another challenge is to be able to ensure the reproducibility of the measurements. In fact, to perform these measurements, the aluminium foils shown in Figure 3.3 are removed and the setup is applied. This, therefore, implies the need to disassemble and reassemble the FeSi core several times during the entire aging cycle and this must not affect the measurements.

The idea for the construction of the setup is to create a structure that ensures that the PCB slides evenly over the surface of the PM and at the same time ensures that the FeSi core is always positioned in the same way, thus having the same magnetic circuit at each measurement. This ensures the accuracy and reproducibility of the results. Now the steps that allowed the validation of this structure will be illustrated.

The first setup was built using a 3D printer and the result is shown in Figure 3.8. It consists of two 1 mm thick plastic bars positioned along the long sides of the PCB (y-direction) in order to force the latter to slide straight when subjected to spring action. Then, four more bars are screwed in pairs in a perpendicular direction to the first two in order to secure the PCB around the FeSi core. The main criticality of this configuration is that, while it can ensure that the setup is always positioned in the correct position with respect to the y-direction, it cannot guarantee that the PCB always slides in the same way on the PM surface. In fact, in the considered structure, there is no constraint against sliding in the x-direction (see Figure 3.8) with respect to the position of the iron core.

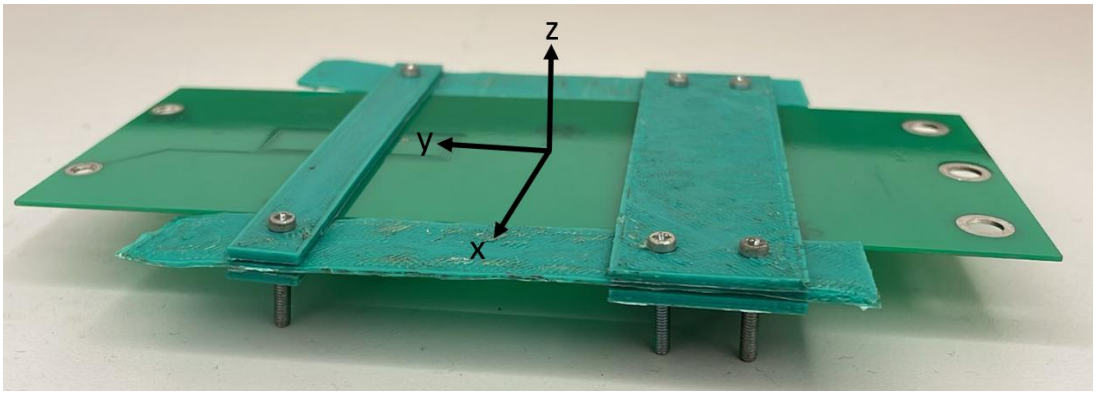

Figure 3.8: First setup prototype used to determine $\langle B_m \rangle$

Another possible criticism of the setup just described is that it does not provide any method for locking the PM at the iron core always in the same position during the tests. Initially, this was not considered to be a major problem because the way the measurements were conducted: each PM was never touched during these phases. However, as it will be shown shortly, an additional structure with this type of functionality was realised later on.

Applying the setup in Figure 3.8 to the core in which the PM is applied, initial tests were then conducted to assess its goodness. The first voltage pulse obtained and then processed via MATLAB is shown in Figure 3.9. It can be seen that in the last part of the graph, the voltage value has an oscillatory trend. This is caused by the fact that, due to the action of the spring, the PCB does not stop immediately but has small rebounds before the spring completely loses its energy. However, this part of the graph is of no interest because it has no influence on what one wants to observe.

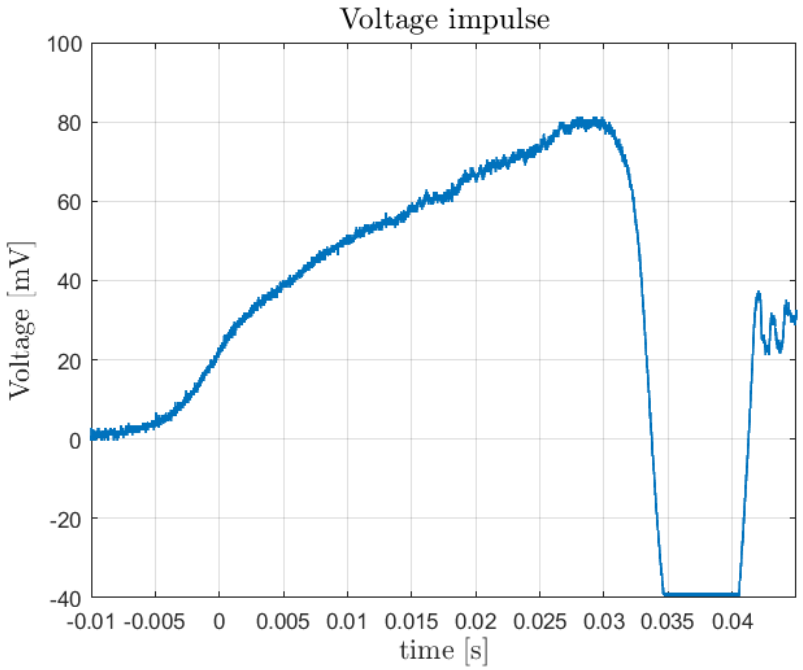

Figure 3.9: First voltage impulse obtained

In order to define the quality of the setup, several experiments were conducted in which the core was assembled and disassembled and evaluations were performed by analysing the measurements obtained. At the end of this process, a dataset of 75 measurements from 5 different experiments was obtained, the results of which are shown in Figure 3.10, and it was possible to make evaluations about the accuracy and robustness of the setup.

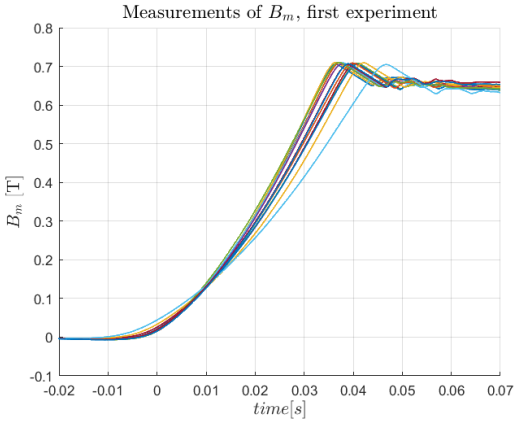

(a) First experiment

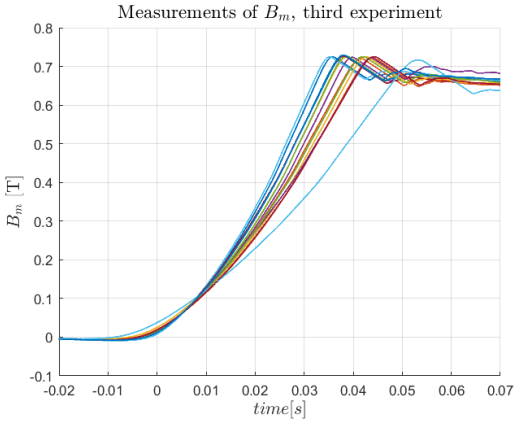

(b) Second experiment

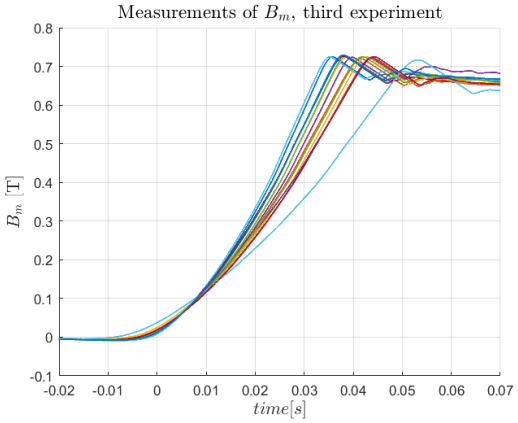

(c) Third experiment

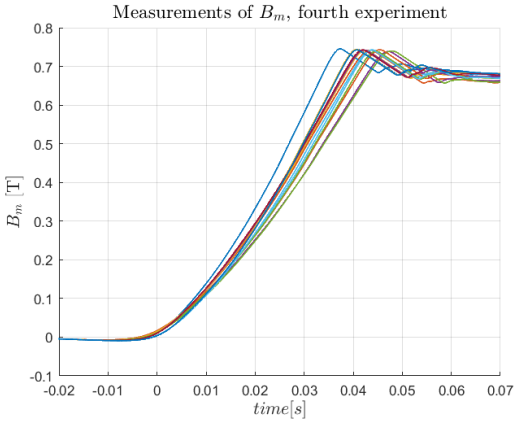

(d) Fourth experiment

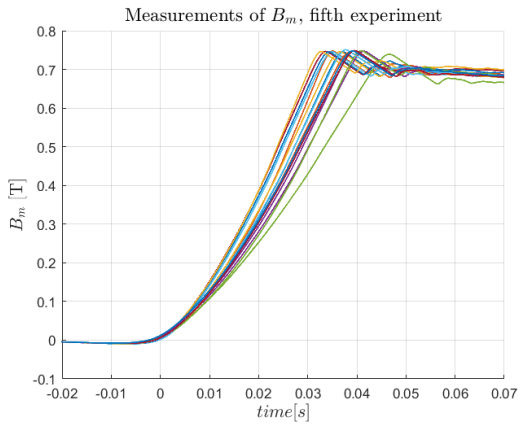

(e) Fifth experiment

Figure 3.10: Results of the five experiments

The relevant value is the one taken by $B_m(t)$ at its peak, as it represents $\langle B_m \rangle$. In Table 3.5 the main parameters considered for the evaluation of the setup are condensed.

Table 3.5: Analysis of the measurements to evaluate the setup

Experiment	$\langle B_{m,max} \rangle$ [T]	$\langle \overline{B_m} \rangle$ [T]	$\sigma_{\%}$ [%]	$\sigma_{\%,total}$ [%]
First	0.7107	0.7076	0.27	2.16
Second	0.7523	0.7489	0.26	
Third	0.7288	0.7242	0.42	
Fourth	0.7455	0.7423	0.27	
Fifth	0.7509	0.7462	0.34	

Where $\langle B_{m,max} \rangle$ represents the maximum value taken by $\langle B_m \rangle$ among the 15 measurements of each experiment, $\langle \overline{B_m} \rangle$ represents the average value among the 15 measurements of each experiment, $\sigma_{\%}$ represents the percentage standard deviation between the measurements of each experiment and $\sigma_{\%,total}$ represents the standard deviation between the 75 measurements of the entire dataset considered.

The results show that the setup is valid in terms of measurement quality when one considers the experiments taken individually. In fact, a percentage standard deviation $\sigma_{\%}$ ranging between 0.26% and 0.42% is accurate enough for the purpose. However, the Table 3.5 highlights a major problem with the current structure: considering the 75 total measurements, the percentage standard deviation $\sigma_{\%,total}$ is 2.16%. Recalling that the expected aging of PMs between 100 and 200 hours in our case can vary between 1% and 3%, the current setup cannot be considered suitable and it must be improved, this is what is going to be discuss now.

From the results obtained, it is clear that the realized structure has the potential to be applied, the key point to be solved now is to make sure that it can guarantee the same test conditions even between experiments, which is not the case with the current setup. Instead of improving the existing setup, it was decided to build a new one that has the same working principle, it is shown in Figure 3.11

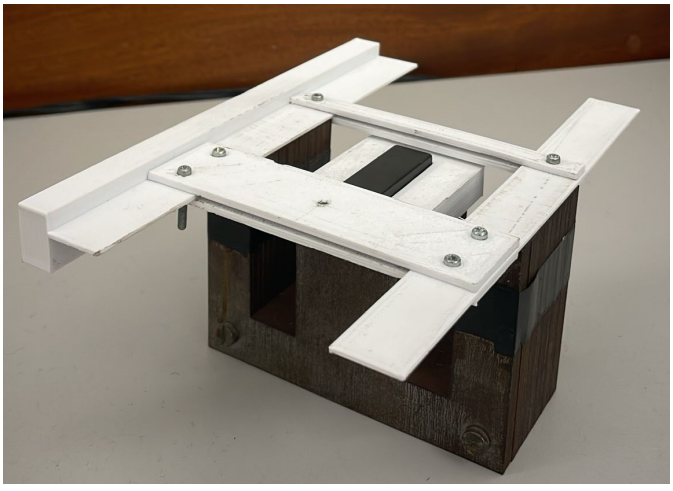

Figure 3.11: New prototype used to determine $\langle B_m \rangle$

As noted, one of the plastic bars located on the long side of the PCB has been replaced by a ”T” plate. The goal is to always ensure the same magnetic circuit by making sure that both the top and bottom of the core are in contact with the latter. This also ensures, with greater precision than before, that the PCB always runs in the same way with respect to the PM surface. In addition, a kind of cover was also produced for the PM for the purpose of protecting it from unwanted movements that would distort the results. To evaluate actual improvements in measurement precision, several tests were performed with the same methods as previously adopted for the first setup. In addition, to get an even more general overview, the tests were performed on two different days. For each of the two days, 30 measurements were performed spread over 3 experiments of 10 each, for a total of 60 measurements. The results are shown in Figures 3.12 and 3.13 and in the summary Table 3.6.

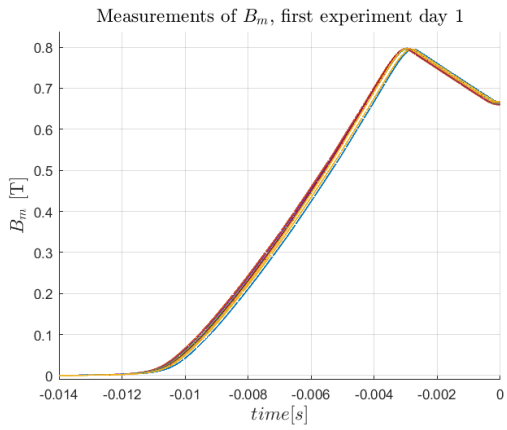

(a) First experiment

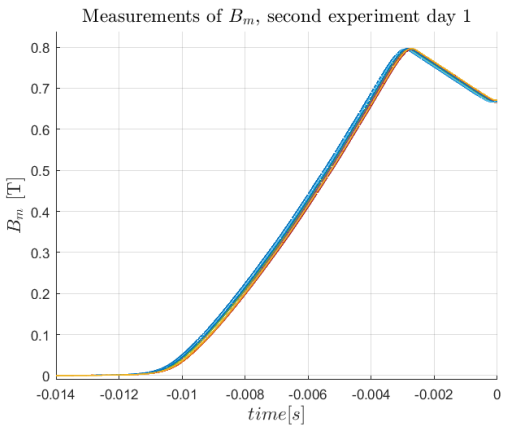

(b) Second experiment

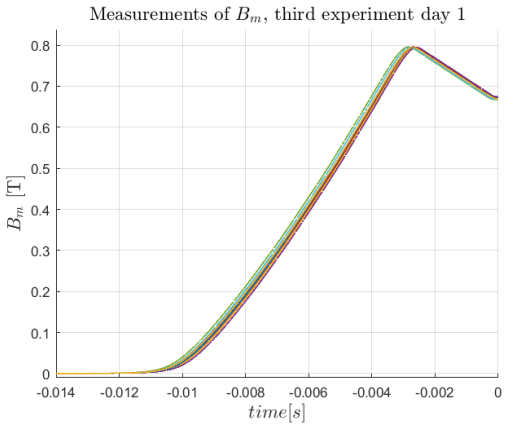

(c) Third experiment

Figure 3.12: Results of the experiments for the new setup during day1

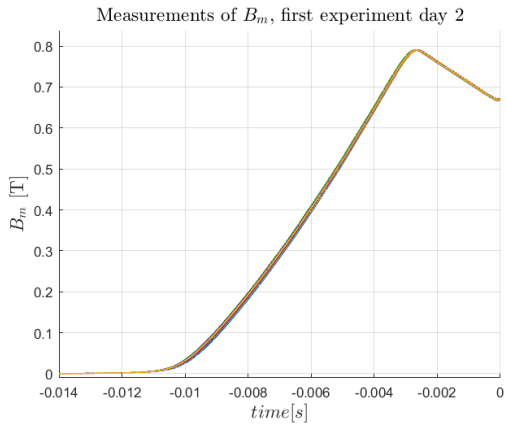

(a) First experiment

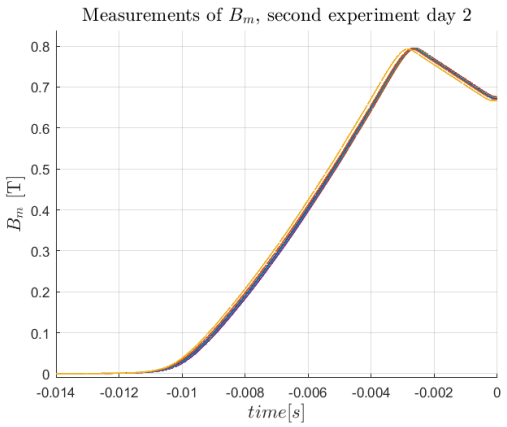

(b) Second experiment

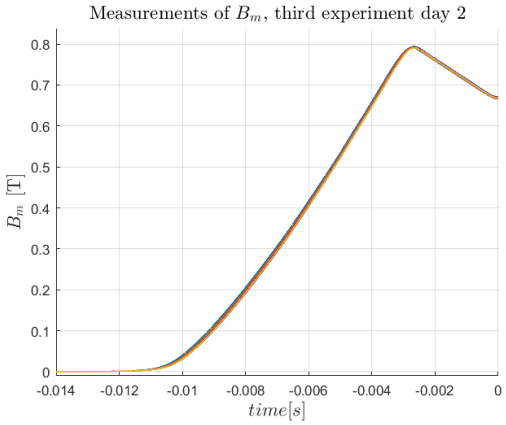

(c) Third experiment

Figure 3.13: Results of the experiments for the new setup during day2

Table 3.6: Analysis of the measurements to evaluate the new setup

Experiment	Day	$\langle B_{m,max} \rangle$ [T]	$\langle \overline{B_m} \rangle$ [T]	$\sigma_{\%}$ [%]	$\sigma_{\%,day}$ [%]	$\sigma_{\%,total}$ [%]
First	1	0.7974	0.7961	0.13	0.15	0.27
Second	1	0.7969	0.7953	0.13		
Third	1	0.7956	0.7943	0.11		
First	2	0.7911	0.7901	0.06	0.23	
Second	2	0.7951	0.7942	0.11		
Third	2	0.7943	0.7925	0.11		

From the results shown in Table 3.6, it is evident that the new setup ensures greater precision during individual experiments: the $\sigma_{\%}$ now oscillates between 0.06% and 0.13%. More importantly, the setup proved robust against repeated assembly and disassembly. In fact, the parameter $\sigma_{\%,day}$ represents the percentage standard deviation among the 30 measurements obtained in the 3 experiments on a given day and as can be seen is 0.15% for day 1 and 0.23% for day 2. Finally, the parameter $\sigma_{\%,total}$

represents the percentage standard deviation among the measurements of the entire dataset under consideration. Observing that this value is 0.27%, it can be concluded that the setup is robust even in the case of variations in the test conditions (e.g. room temperature), as half of the measurements were obtained on one day, and the other half on another. A final important observation is that the values of $\langle B_{m,max} \rangle$ and $\langle \overline{B_m} \rangle$ for each experiment in the new setup are higher than each of the experiments in the previous setup. This suggests that a condition has now been reached whereby the PCB slides more precisely with respect to the PM surface.

The structure met the accuracy and reproducibility requirements initially set and was therefore applied during the thermal aging cycle discussed in the next section.

3.4 Thermal aging cycle procedure

Having defined and evaluated the method to derive $\langle B_m \rangle$, it is now time to apply it in between the thermal cycle phases to analyse the behaviour of PMs. The thermal cycle is divided into six phases in which the structure composed by the FeSi core and the PM is placed in the oven as illustrated in Figure 3.14. During this phase, the OV301 industrial oven was used for the first two tests (1h and 5h), whose datasheet can be found in Appendix D. For the subsequent measurements, due to logistical problems in the laboratory where the oven was located, another oven was used [35].

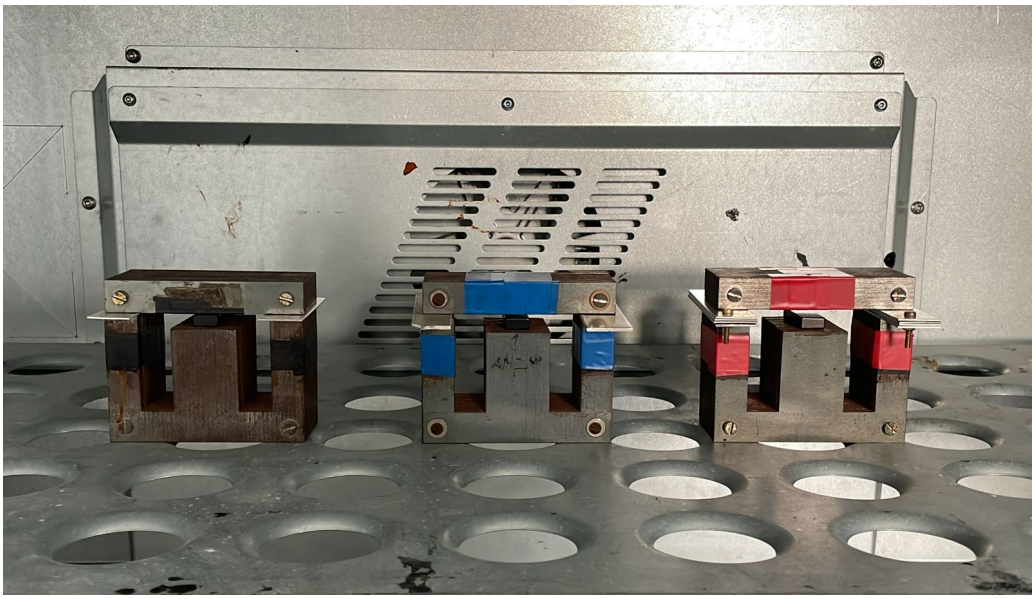

Figure 3.14: BMN-42SH samples in oven with different air gaps

Each phase is longer than the previous one, for a total of 186 hours. Following a detailed analysis of the literature, and considering the tests carried out by my colleagues before me, it was decided to perform the aging tests at a temperature of 140℃. During the experiments, the three BMN-42SH samples (PM1, PM2, PM3) were placed in the oven simultaneously to ensure uniformity in the test and measurement conditions. Following unexpected results, a further test was then performed on sample PM2, this decision will be motivated in the next section. A further thermal cycle of 186 hours was also

performed on sample PM4 of grade BMN-48SH according to the same methodology just described, in order to clarify the results obtained for samples PM1, PM2 and PM3. Figure 3.15 summarizes what has just been explained.

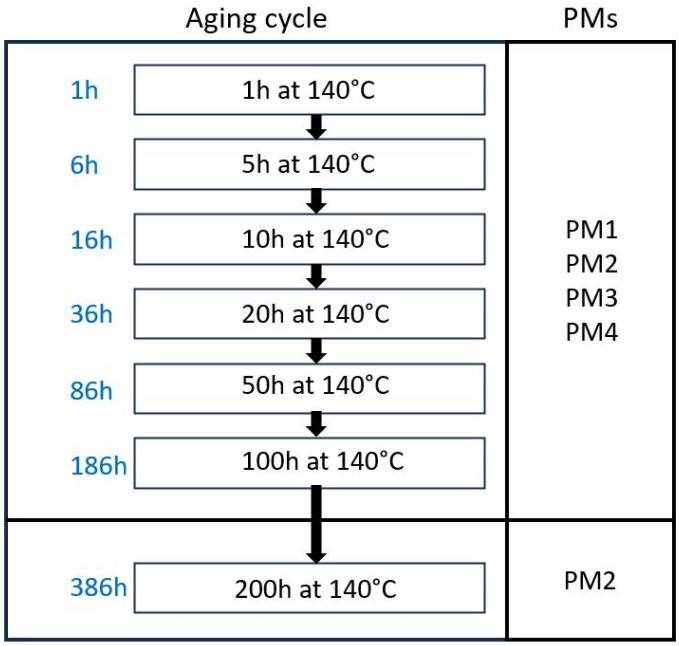

Figure 3.15: Aging cycle performed

3.5 Thermal aging cycle results for BMN-42SH

The thermal cycle discussed in the previous section was therefore applied to the NdFeB BMN-42SH magnets codenamed PM1, PM2 and PM3 (see Table 3.2). This section is dedicated to the analysis of the results obtained for the three samples during the various phases of the cycle.

3.5.1 PM1 analysis

The PM1 sample was aged using an aluminium air gap of 1mm, resulting in a PC of approximately 4.5. For each of the cycle phases a procedure similar to that carried out during the validation of the setup was applied: three experiments of 10 measurements each were conducted, interspersed with core disassembly and reassembly operations, for a total of 30 measurements. Table 3.7 summarises the main parameters taken into account to conduct the analysis of the results.

Table 3.7: Parameters to consider, PM1

	0h	1h	6h	16h	36h	86h	186h
$\langle B_m \rangle$ [T]	[0.8425-0.8363]	[0.8365-0.8309]	[0.8390-0.8350]	[0.8451-0.8427]	[0.8373-0.8318]	[0.8477-0.8461]	[0.8394-0.8315]
$\sigma_{\%}$ [%]	0.19	0.13	0.3	0.07	0.18	0.04	0.3

The first is obviously the value that $\langle B_m \rangle$ takes during each phase. A range is indicated in the table and the limit values represent the maximum and minimum obtained among the 30 measurements. The second is instead the percentage standard deviation $\sigma_{\%}$, used to evaluate the criteria of precision and reproducibility discussed above. At the end of the last aging phase, this sample was the only one to show damage on its surface, as highlighted in Figure 3.16.

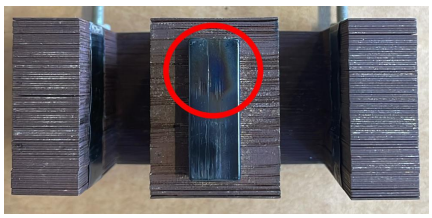

Figure 3.16: Damage after 100h on PM1 surface

However, as can be seen from Table 3.7, this would only appear to be damage to the magnet's coating, as no particularly appreciable losses were noted during this measurement phase.

A first observation is that, for each phase, the $\sigma_{\%}$ amply satisfies the established criteria, with values ranging between 0.04% and 0.3% considering the total number of measurements acquired. A problem may arise from the fact that the smallest standard deviation is about 7 times lower than the largest one. Obviously, in order to have uniformity of results one would like to ensure that $\sigma_{\%}$ is as similar as possible in each experiment, however, it must be considered that the percentages in question are close to zero. and even the slightest misplacement of the setup can have a major impact on the result. It should also be considered that, despite this diversity in the quality of the measurements, even the worst situation (0.3%) meets the criteria to consider the data acquired acceptable.

During each experiment, the ambient temperature was recorded and the values of $\langle B_m \rangle$ given in Table 3.7 were normalised with respect to this factor according to the datasheet of Appendix A. The box plot of Figure 3.17 was then created to provide a graphic display of the PM1 behaviour over time, in which all the measurements obtained are illustrated.

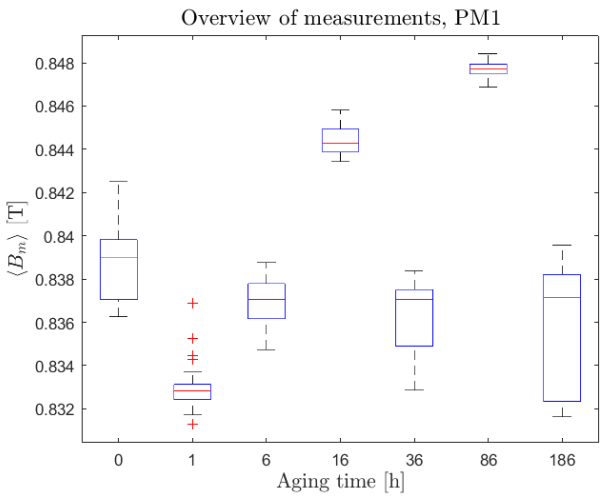

Figure 3.17: Overview of the measurements for PM1

What is immediately evident when analysing the Figure 3.17 is that the PM1 sample does not appear to age over time but rather, it seems that $\langle B_m \rangle$ oscillates around a certain value.

The next step is to decide how to treat these measurements to rigorously define the behaviour of PM1. In general, when a group of values is available, it is good practice to consider the average one to be analysed. In order to apply this concept to our case in a meaningful way, one should ensure the same distribution of measurements at each stage of the cycle. To evaluate this possibility, a comparison of the distribution of measurements during two different experiments is presented in Figure 3.18.

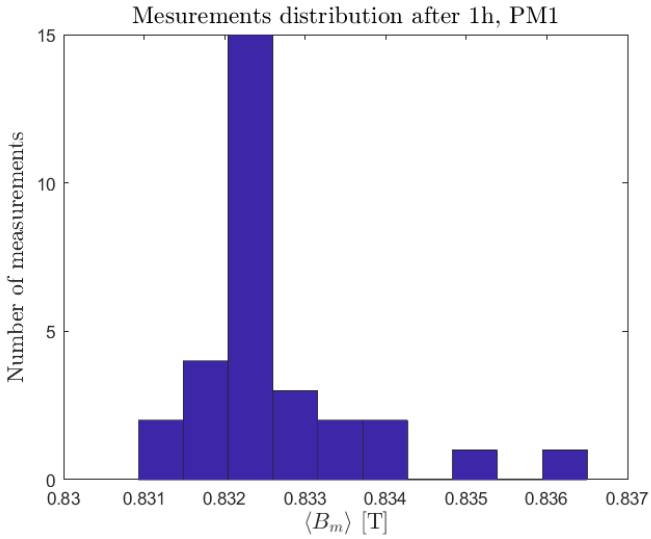

(a) Distribution of measurements, 1h

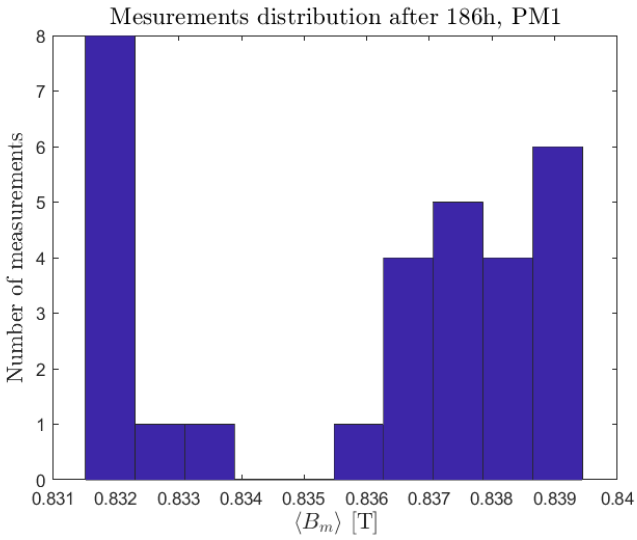

(b) Distribution of measurements, 1h

Figure 3.18: Comparison of the distribution of measurements in different experiments

As can be seen, in Figure 3.18(a) most of the measurements are shifted towards the lower end of the range, whereas in Figure 3.18(b) it is the exact opposite. This implies that in the two cases the mean value of the magnetic flux $\langle \overline{B_m} \rangle$ does not fit equally in the range of values. Not being able to ensure the same distribution between the measurements, it was assessed that it did not make sense to consider

$\langle \overline{B_m} \rangle$ in order to study the behaviour of PM1; on the contrary, it would be detrimental to a correct analysis of the results.

It was therefore concluded that the best method for accurately assessing aging was to consider the maximum value assumed by $\langle B_m \rangle$. In fact, this value represents the condition for which the PCB coil most accurately slid over the surface of the sample among the 30 measurements of the stage considered.

Starting from Figure 3.17 and considering what had just been decided, the logarithmic scale graph of Figure 3.19 was made and from this, conclusions were drawn regarding the behaviour of PM1. The graph represents the losses of $\langle B_m \rangle$ during the aging cycle. For example, at the i-th stage of the cycle, the magnetic flux loss is calculated as follows:

$$loss_{\%,i} = -\left(1 - \frac{\langle B_{m,i} \rangle}{\langle B_{m,0} \rangle}\right) \cdot 100 \tag{3.5}$$

Where $\langle B_{m,0} \rangle$ is the average magnetic flux before the first aging phase, $\langle B_{m,i} \rangle$ is the one at the i-th phase and the result is multiplied by 100 to obtain a percentage value.

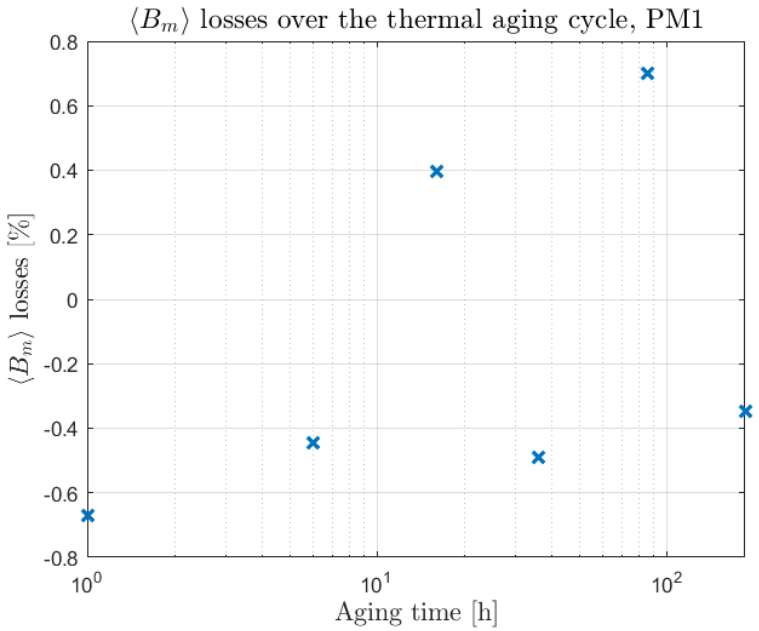

Figure 3.19: PM1 behaviour over the cycle

From Figure 3.19 it can be seen that, following an initial phase in which the magnet appears to age, $\langle B_m \rangle$ begins to oscillate around a certain value. At some stages, the magnet even appears to rejuvenate, in fact the losses take on a positive value. At the end of the cycle, PM1 appears to have aged by only 0.35%, which can be interpreted as the sample not having aged at all.

This was not an expected result, neither by the reviewed literature nor by logic. At this point, it is necessary to evaluate the behaviour of the other two samples, PM2 and PM3, in order to draw some conclusions.

3.5.2 PM2 and PM3 analysis

The previous subsection provided in detail the method of analysing the results for PM1. In order to have comparable results, the same evaluation criteria were also maintained for the other two samples. It is for this reason that this subsection is devoted to analysing the results of samples PM2 (2mm air gap) and PM3 (4mm air gap) at the same time. It is important to highlight that each phase conducted on PM1, aging and measurements, was carried out simultaneously on samples PM2 and PM3 in order to have uniformity in the test conditions. Tables 3.8 and 3.9 summarise the results obtained for PM2 and PM3, respectively.

Table 3.8: Parameters to consider, PM2

	0h	1h	6h	16h	36h	86h	186h
$\langle B_m \rangle$ [T]	[0.7967-0.7916]	[0.7930-0.7869]	[0.7919-0.7893]	[0.7941-0.7905]	[0.7883-0.7845]	[0.7971-0.7944]	[0.7920-0.7879]
$\sigma_{\%}$ [%]	0.13	0.25	0.09	0.14	0.13	0.10	0.12

Table 3.9: Parameters to consider, PM3

	0h	1h	6h	16h	36h	86h	186h
$\langle B_m \rangle$ [T]	[0.8099-0.8020]	[0.8084-0.8057]	[0.8053-0.7992]	[0.8108-0.8085]	[0.8094-0.8038]	[0.8136-0.8109]	[0.8125-0.8003]
$\sigma_{\%}$ [%]	0.31	0.07	0.24	0.09	0.17	0.10	0.55

These tables should be interpreted in the same way as Table 3.7. Again, the quality of the measurements can be considered sufficiently good for the imposed objective. For PM2 the percentage standard deviation $\sigma_{\%}$ fluctuates between 0.09% and 0.25%, while for PM3 it fluctuates between 0.07% and 0.55%. The problem of not being able to guarantee the same level of accuracy is also evident for PM2 and PM3. At the same time, as explained above, one has to deal with percentages close to zero and therefore easily perturbed. Furthermore, it should be considered that the value $\sigma_{\%}$ = 0.55%, which is the worst accuracy recorded, is to be regarded as an isolated case. In fact, if one does not consider this value, the maximum percentage standard deviation had been 0.31% considering all experiments performed for the three samples. Since the worst accuracy was recorded for the very last experiment performed (after 186h of PM3), this could indicate a degradation of the measurement setup e.g. caused by a loosening of the screws.

Note the fact that the initial value of $\langle B_m \rangle$ for both PM2 and PM3 was about 0.04T lower than that of PM1. This could mean one of two things: that PM2 and PM3 were in a higher state of aging from the start, and could therefore affect the results of the thermal cycle, or simply that it was just a manufacturing defect which is not supposed to affect the results. As will be explained shortly, since the three samples had the same behaviour throughout the cycle, one is led to validate the second hypothesis. In fact, if it had been due to the fact that the samples were in a different state of aging, different behaviour would have been observed during the cycle.

As for PM1, during each experiment, the ambient temperature was recorded and the values of $\langle B_m \rangle$

given in Tables 3.8 and 3.9 were normalised with respect to this factor according to the datasheet of Appendix A. The box plots in Figure 3.20 and 3.21 were therefore created to provide a graphical visualisation of the behaviour over time of PM2 and PM3 respectively, in which all the measurements obtained are illustrated.

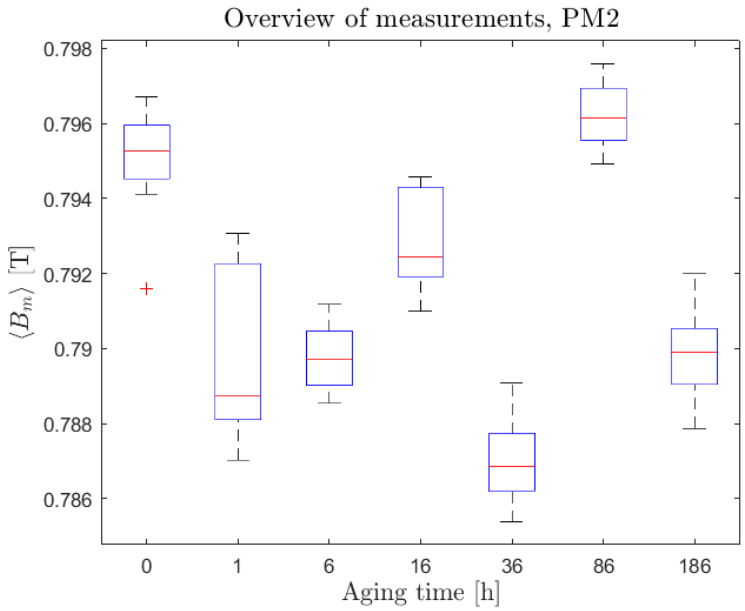

Figure 3.20: Overview of the measurements for PM2

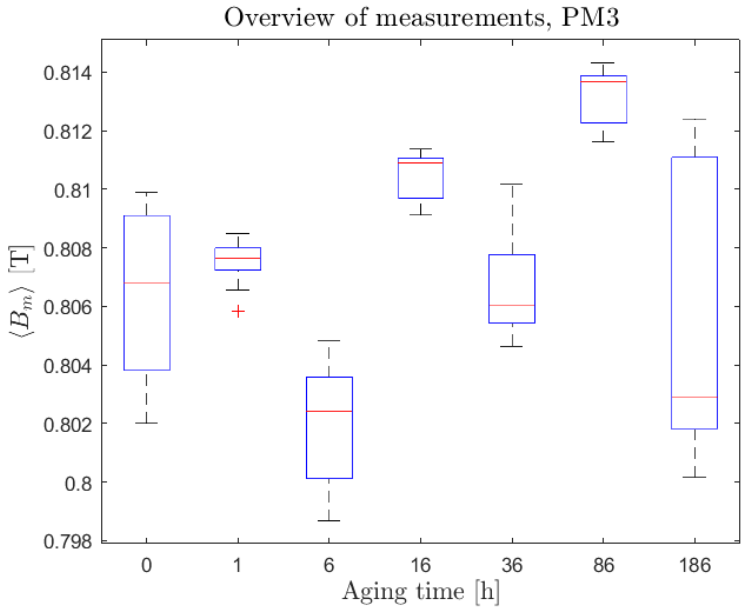

Figure 3.21: Overview of the measurements for PM3

In both Figures it can be observed that the samples do not age but rather have an oscillatory behaviour throughout the thermal cycle, as already seen for PM1. For the same reasons listed in the previous subsection, it was decided to consider the maximum value assumed by $\langle B_m \rangle$ for studying the aging of PM2 and PM3.

From the consideration just made, the graphs in Figure 3.22 and 3.23 were produced for PM2 and PM3 respectively. They were made on a logarithmic scale to better visualise the behaviour of the two samples.

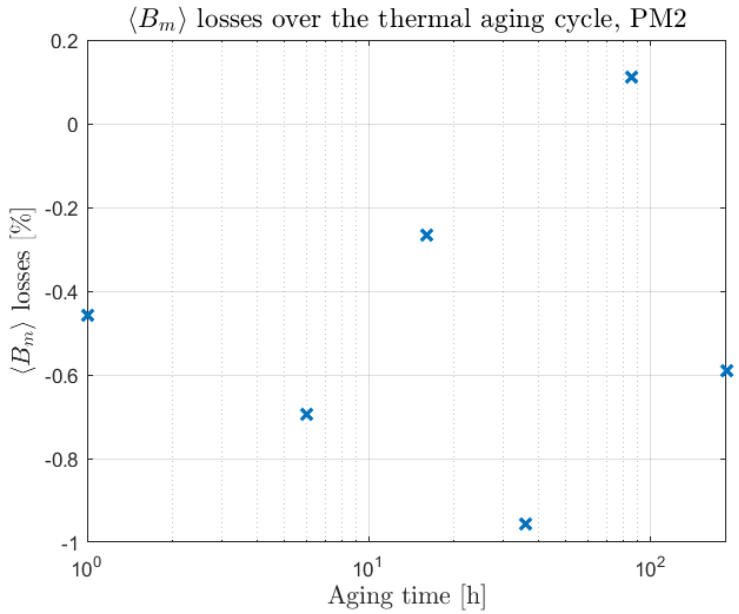

Figure 3.22: PM2 behaviour over the cycle

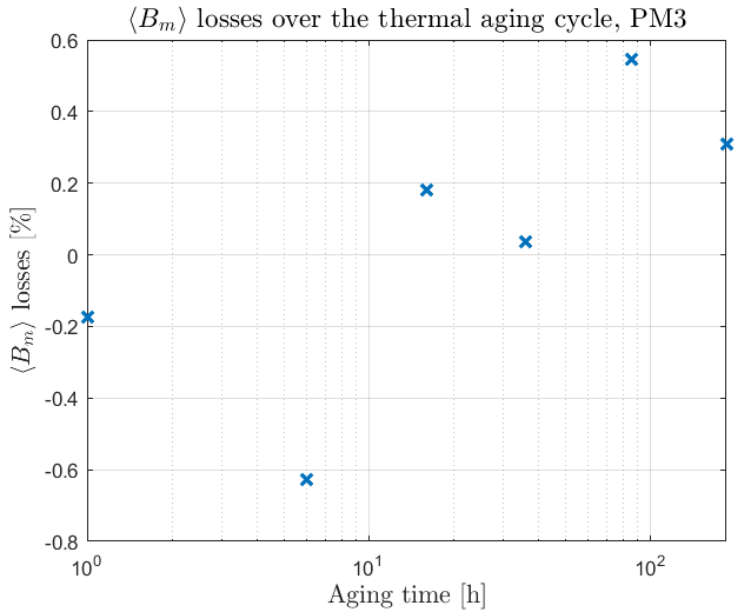

Figure 3.23: PM3 behaviour over the cycle

From this graphs, it is evident that both PM2 and PM3 have a similar behaviour to that observed in Figure 3.19 for PM1. It is therefore clear that unexpected results in terms of aging were obtained for all the samples analysed. For clarity, the losses of $\langle B_m \rangle$ at the end of the aging cycle are summarized in Table 3.10.

Table 3.10: Losses at the end of the aging cycle for the three samples

	PM1	PM2	PM3
$\langle B_m \rangle$ losses [%]	-0.35	-0.59	+0.31

This table shows that no sample has aged and even PM3 appears rejuvenated compared to the beginning of the cycle. However, there are factors that indicate that this could be a true trend in the behaviour of the samples and not measurement errors of $\langle B_m \rangle$. To feed this theory it is useful to observe Figure 3.24.

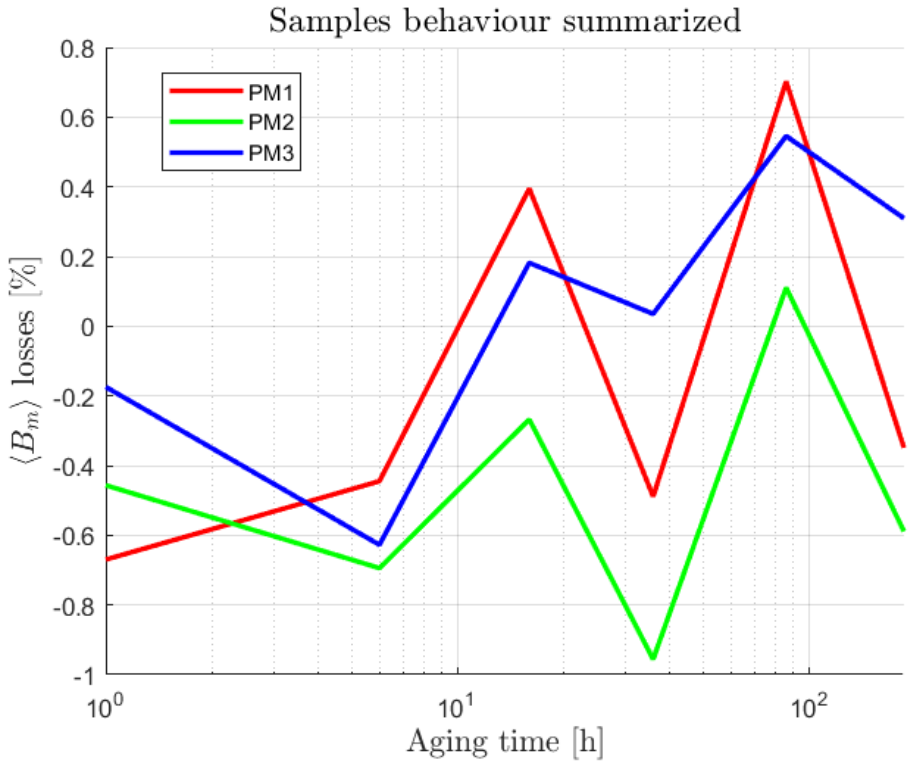

Figure 3.24: Recap of the behaviour of the three samples analysed

Analysing Figure 3.24 it evident how the three samples appear to age and rejuvenate during the same phases and it is statistically unlikely that the same errors were made at each stage of the cycle for each of the three samples.

Furthermore, it can be seen that PM3 tends to have a higher value than initially assumed at almost all stages of the cycle.Since this sample was aged with the thickest air gap among the three samples, a more pronounced aging was all the more expected from the literature reviewed.

Considering what just obtained, it was necessary to make assumptions regarding possible justifications for the unexpected results. At first, it was thought that the temperature of the room could have a greater impact than the datasheet in Appendix A. For this reason, a brief study was conducted in this regard, illustrated in the next section.

3.5.3 Study on influence of room temperature

To try to justify the unexpected results obtained, a study was conducted to determine the real effect of temperature on the PM $B(H)$ curve. In fact, the datasheet of Appendix A indicates that the PM remanence B_r can vary by up to -0.12%/℃, and an attempt was made to find out whether this is actually the case in reality.

During the test, the iron core with a PM (already aged) applied and without any artificially introduced air gap was placed in the oven. At this point, the gaussmeter of Appendix C was placed just above the surface of the PM. An attempt was made to place it in as central a position as possible, but the important thing in order to obtain consistent results is that the position remains the same throughout the experiment. Then a temperature sensor was placed as close as possible to the PM and the test could begin.

From 18℃ to 26℃ at 1℃ intervals, the value taken by the gaussmeter was recorded. This temperature range was chosen because it was considered realistic with respect to typical test conditions. In fact, it should be remembered that the measurements were performed at room temperature and therefore it does not make sense to go higher than 26℃. In addition, in order to give the core and magnet time to reach the desired temperature, each step lasted 45 minutes, making a total of 6 hours and 45 minutes. In this way, the results obtained can be considered consistent. The values recorded are represented in the graph of Figure 3.25.

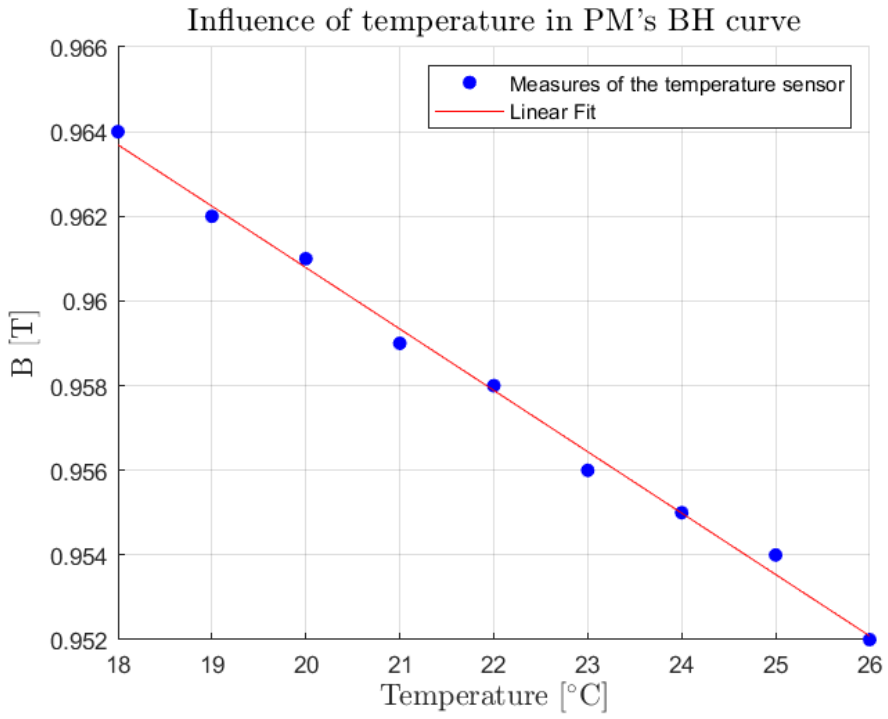

Figure 3.25: Relation between B and temperature

In this graph, the red line (linear fit of the recorded points) represents how temperature affects the magnetic flux of the PM, and the experimentally obtained result is -0.145%/℃, which is close to the

value given in the datasheet. It should also be considered that the study conducted may have been influenced by errors I made unintentionally during the measurements and limitations of the equipment used. Furthermore, the datasheet refers to the variation of B_r whereas the data collected by gaussmeter represents the value assumed by a point of the PM for a specific PC. These two values are close to each other but not the same, which is also why the result obtained is not exactly the same as the datasheet.

Finally, for feedback, the behaviour of the three samples was plotted when the correction factor considered was the one obtained experimentally during the study just conducted (-0.145%/℃ instead of -0.120%/℃ as indicated on the datasheet). The result is shown in Figure 3.26.

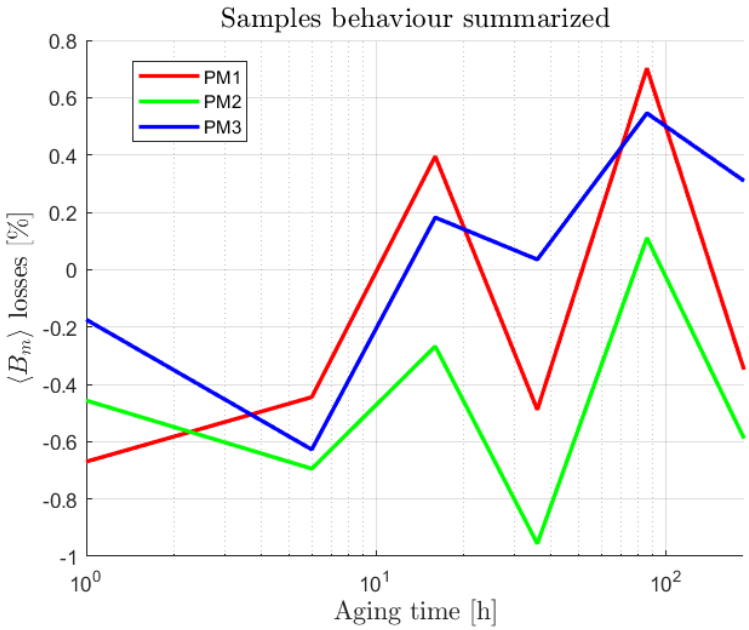

Figure 3.26: Behaviour of PMs considering the real correction factor

As can be seen, this graph is virtually identical to Figure 3.24. This consideration was helpful in demonstrating that the impact of temperature is not as influential on the $B(H)$ curve as hypothesised, and that the cause of the unexpected results must therefore be sought in other factors.

3.5.4 Additional test for PM2

Having validated the fact that room temperature is not a heavy influencing factor in the measurements made during the tests, another hypothesis must be formulated to explain how the results that were obtained are not in line with expectations.

It was assumed that the PMs may have already aged at room temperature, as there is no certainty as to the origins of these. The results reported for the three samples of BMN-42SH show that $\langle B_m \rangle$ seems to stabilise around a certain value without the PMs aging. This could mean that the aging stage of the analysed PMs is already advanced with respect to the origin of the logarithmic scale and that therefore a thermal cycle of 186 hours is not sufficient to reveal aging. For this reason, an additional 200-hour oven

phase was introduced on the PM2 sample, for a total of 386 hours of aging. The aim was to observe whether $\langle B_m \rangle$ continued to oscillate, thus lending credibility to the hypothesis formulated.

The results presented in Figure 3.27 seem to confirm the theory that the PMs tested may have already been at an advanced stage of aging. In fact, even after 386 hours, the sample does not appear to have aged appreciably. In order to fully prove this theory, it is necessary to test other PMs that are confirmed to have not aged. A positive result would prove that the method applied is valid and that the samples PM1, PM2 and PM3 had already aged before the thermal cycle.

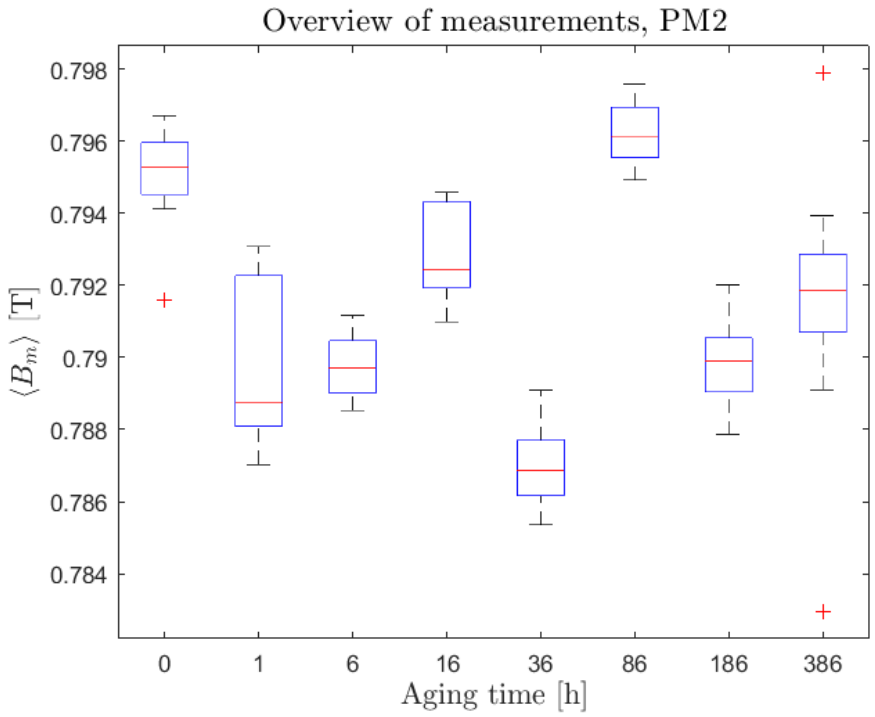

Figure 3.27: Overview of the measurements for PM2, after the 200h phase

3.6 Thermal aging cycle results for BMN-48SH

With the aim of understanding the reasons for the results obtained during the aging tests performed and at the same time demonstrating the actual validity of the methodology employed, it was decided to carry out the tests on a sample of BMN-48SH, codenamed PM4. It has been aged for a total of 186 hours at a PC approximately equal to 2.3.

Before illustrating the results obtained it should be considered that the setup was tailor-made for BMN-42SH samples, as the use of BMN-48SH sample was not initially planned. For example, the dimensions of the coil, as explained in 3.2, are such that it runs exactly on the surface of a BMN-42SH sample, avoiding leakages. Obviously, since the sample of BMN-48SH has different dimensions, this condition does not occur in this case. However, this is not a problem: the aim is simply to obtain reliable measurements of $\langle B_m \rangle$. If the same sliding condition is guaranteed for each measurement, it is sufficient to apply the method to the aging tests for sample PM4.

For each of the cycle phases three experiments of 10 measurements each were conducted, interspersed with core disassembly and reassembly operations, for a total of 30 measurements, as done for samples PM1, PM2 and PM3. The collected data were normalised with respect to temperature according to the datasheet of Appendix B and summarised in Table 3.11.

Table 3.11: Parameters to consider, PM4

	0h	1h	6h	16h	36h	86h	186h
$\langle B_m \rangle$ [T]	[0.6285-0.6158]	[0.6296-0.6283]	[0.6313-6276]	[0.6303-0.6271]	[0.6311-0.6288]	[0.6311-0.6258]	[0.6312-0.6292]
$\sigma_{\%}$ [%]	0.42	0.05	0.16	0.18	0.12	0.18	0.10

From the Table, it can be seen that the $\langle B_m \rangle$ values for PM4 are lower than those recorded for PM1, PM2 and PM3, and this is solely due to the consideration made earlier that the setup was tailor-made for BMN-42SH samples. It is clear that the objective of obtaining precise and reproducible measurements has been achieved. The $\sigma_{\%}$ fluctuates between 0.05% and 0.42% and it must also be considered that the latter value may have been caused by human error in the measurements as it is larger than all the other ones.

The results shown in Table 3.11 show that the sample has not aged. To clarify this, the data have been plotted in the box plot in Figure 3.28.

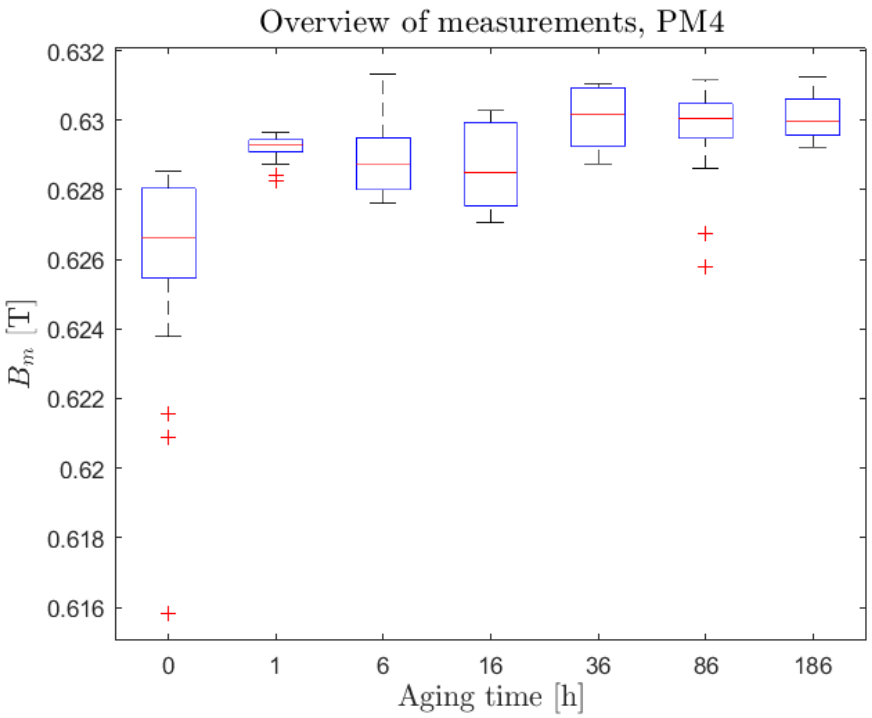

Figure 3.28: Overview of the measurements for PM4

The box plot highlights the fact that PM4 has not aged during the entire cycle. In fact, it is observed that $\langle B_m \rangle$ is not affected during the entire thermal cycle. This is a similar result to that obtained during the tests for the three BMN-42SH samples. However, if one compares Figure 3.28 with Figures 3.17, 3.20, 3.21 it is evident that this sample has a slightly different behaviour. In fact samples PM1, PM2 and

PM3 were characterised by a $\langle B_m \rangle$ oscillation during the cycle, whereas for PM4 this phenomenon did not occur.

The behaviour of PM4 is more consistent than that seen for PM1, PM2 and PM3, and finding an explanation for this difference is a difficult challenge and requires further testing to be resolved. There are several hypotheses that can be formulated. The first is that, as stated earlier, there is no certainty about the origins of the BMN-42SH samples: their state of aging prior to oven testing was not known precisely and may have influenced the final results. Another factor is that PM4 is of a different grade than the other three samples and may show greater resistance to aging.

However, none of the four samples analysed showed actual aging in line with the State of the Art. This situation is difficult to explain: on the one hand, one is certain that the measurements obtained are true and reliable, on the other hand, the results illustrated during this thesis work go against those obtained in other research. More data would have to be collected in order to be able to state this with certainty, and this process could take months if not years. Since not enough time is available, it was decided to use data previously obtained by a colleague to define the impact of PM aging on an IPMSM. The next Chapter will introduce these data and explain how they were used for the purpose of this thesis.

Chapter 4

Impact of aging on an IPMSM

This Chapter is devoted to the analysis of the effects that aging of permanent magnets (PMs) has on an Internal Permanent Magnets Synchronous Motor (IPMSM). For the analysis that will be shown, since the data obtained in Chapter 3 are not in line with the State of the Art, data previously obtained by a colleague will be used. The analysis will include the study of torque and efficiency variation at the nominal point, at different stages of aging.

4.1 Data and motor overview

As mentioned just above, for simulations using Finite Element Analysis (FEA), data collected during a previous thesis work by a colleague were used [26]. The aging procedure was the same as that followed during this thesis (see Figure 3.15), except that the tests were performed at 100℃ and 120℃. Also, the same aluminum thicknesses were used, consequently obtaining the same Permeance Coefficients (PCs) for the PMs. With the data obtained, the prediction of aging was then performed using an adaptation of the Arrhenius Model, which is shown in Equation 4.1 and represents the losses in the remanence of PMs by comparing them with the value taken before the start of the aging cycle.

$$\frac{B_r(t)}{B_r(t_0)} - 1 = M_0(T, PC) + S(T, PC) ln(\frac{t}{t_0}) \tag{4.1}$$

This equation describes the relative change in remanence B_r over time t, with a dependence on temperature T and the permeance coefficient of the PM, PC. In the equation $M_0(T, PC)$ represents the magnetization, while $S(T, PC)$ is the magnetic viscosity coefficient. For convenience these parameters have been summarized in Table 4.1.

Table 4.1: Arrhenius parameters for N42SH samples

	$M_0(T, PC)$			$S(T, PC)$		
	PC = 4.5	PC = 2.3	PC = 1.1	PC = 4.5	PC = 2.3	PC = 1.1
100℃	-0.169	-0.328	-0.257	-0.367	-0.411	-0.442
120℃	-0.171	-0.338	-0.312	-0.370	-0.438	-0.500

From these data, it was possible to plot a 3-D graph showing how PC affects the aging of PMs in a range of PCs from 1.1 to 4.5. This was made because then, knowing the PC value of the PMs included in the analyzed IPMSM, it will be possible to know their aging status. The two planes obtained for temperatures of 100℃ and 120℃ are shown in Figures 4.1 and 4.2, respectively.

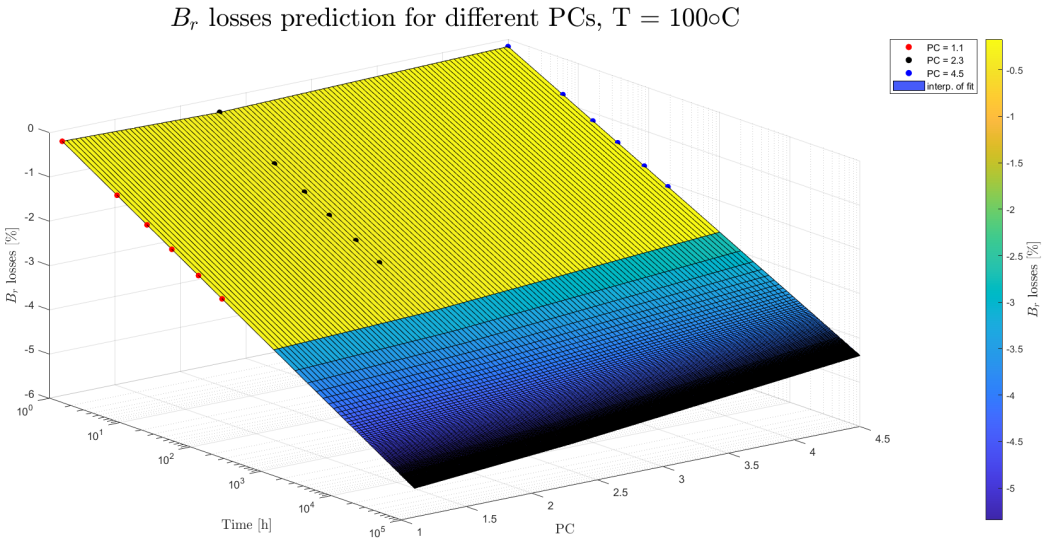

Figure 4.1: Interpolation plane for $B_r(t)$ losses at 100℃

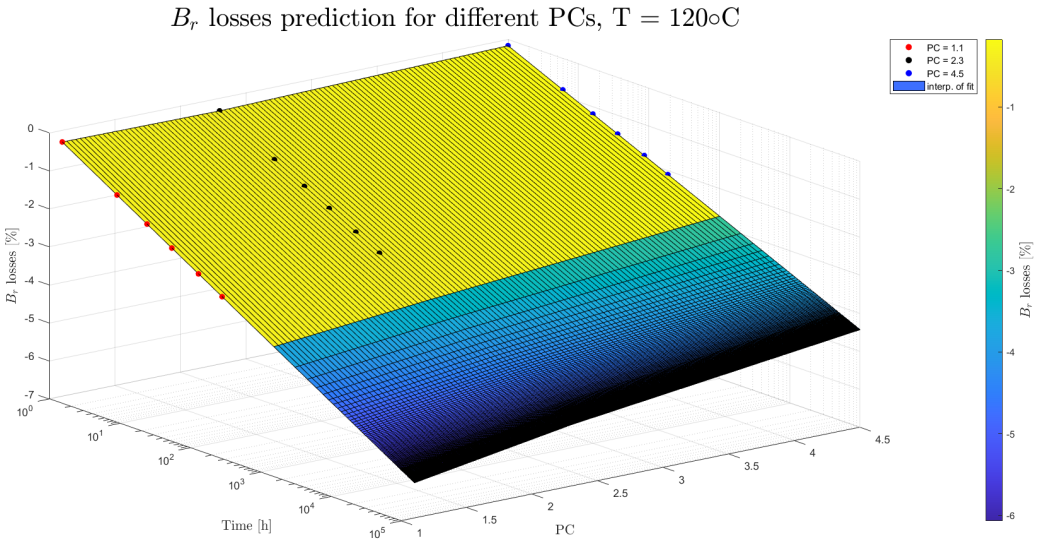

Figure 4.2: Interpolation plane for $B_r(t)$ losses at 120℃

In order to proceed with the analysis, it is necessary to know the electric motor to be studied. It is an IPMSM still under construction at the University's electrical machines laboratory characterized by a rotor in which there are 8 PMs (4 pole pairs), as shown in Figure 4.3.

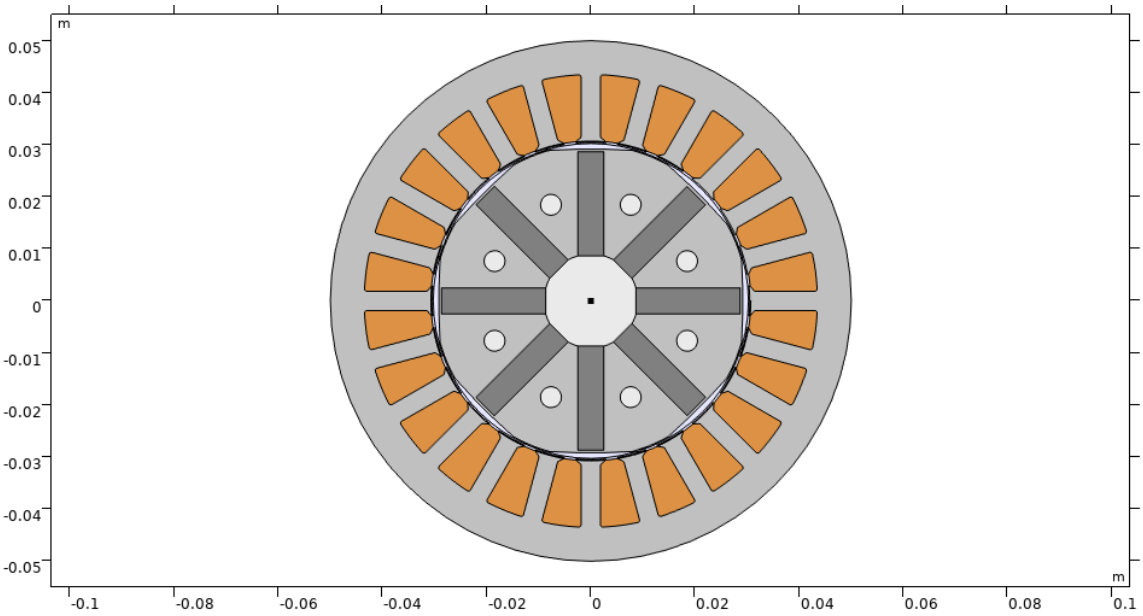

Figure 4.3: Geometry of the IPMSM to be studied

A first simulation was performed to define the average PC (PC_{av}) of the PMs within an electric cycle. As observed in Figure 4.3, because of the geometry of the motor to be studied, each PM is characterized by the same value of PC_{av}. By means of this simulation the Torque-Speed map observed in Figure 4.4 was made and indicates at each point of operation of the motor, the respective value of PC_{av}.

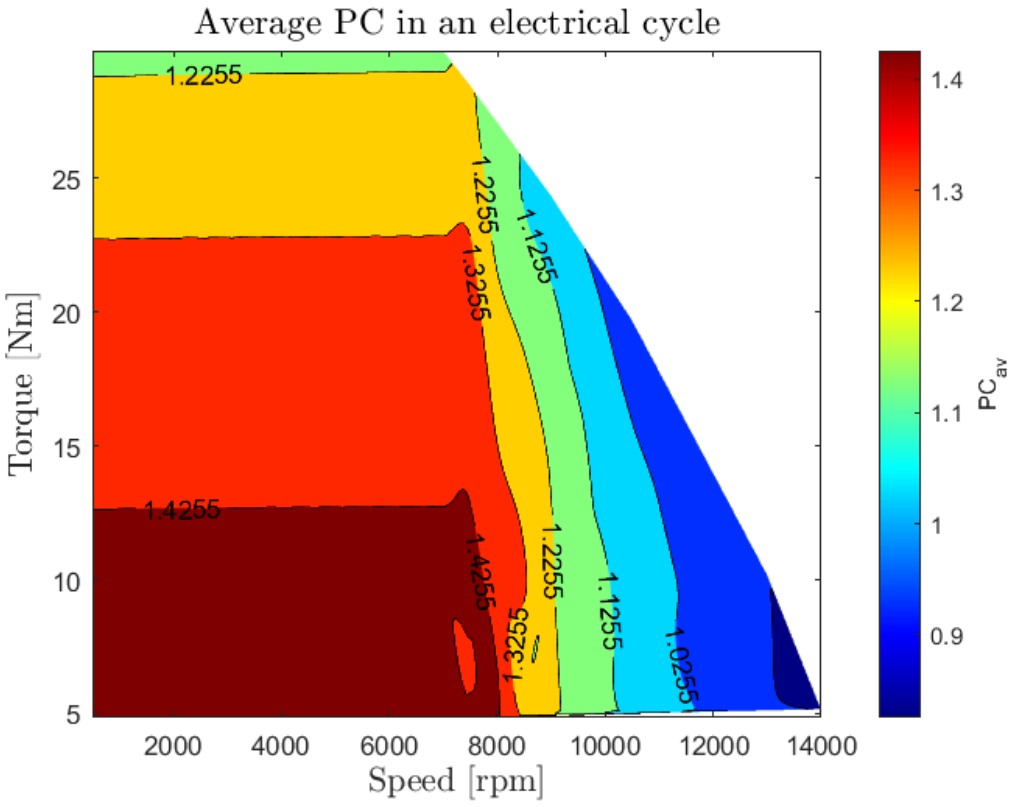

Figure 4.4: Map of the values of PC_{av} for every operating point of the motor

From the map it is clear that, depending on where the motor operates, the PC_{av} value can vary between about 0.9 and 1.45 in an electrical cycle. As can be seen from Figures 4.1 and 4.2, this difference does not have such a major impact on the aging of PMs. However, to conduct an accurate analysis, it is necessary to define a criterion for selecting which value to use for PC_{av}. To do this, it is also necessary to understand how the PC_{av} varies along the PM. Figure 4.5 illustrates the value of PC_{av} along the PM for a certain point of machine operation (nominal torque and speed).

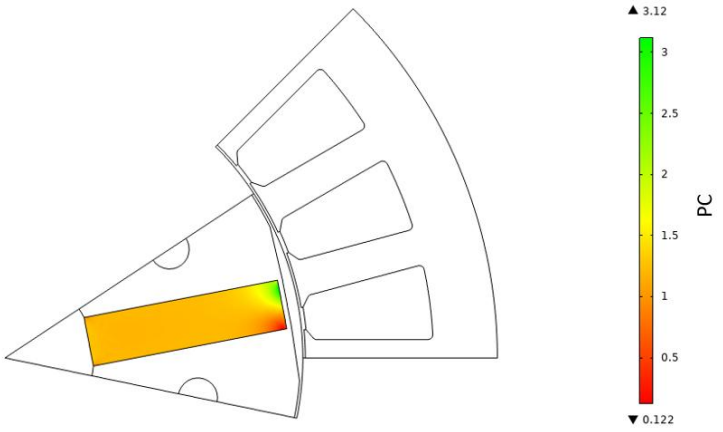

Figure 4.5: Illustration of PC_{av} along a PM

As will be explained in more depth in later sections, the entire analysis is based on studying the nominal point of the motor. The mean value over the PMs is PC_{av} = 1.21 and as a first approach will be considered constant during the aging of the machine, checking later whether this is acceptable.

Before proceeding with the exposition of the results and the analysis, it is necessary to provide an overview of the assumptions made to carry out the study. In fact, a number of simplifications were made to arrive at the final result, and it is important to keep these in mind when evaluating the quality of the results obtained. The main ones are listed below:

1. The PC_{av} of the PMs is constant in an electrical cycle.
2. The PC_{av} of the PMs is constant along their surface.
3. The motor works continuously at the same point of operation.
4. The temperature inside the motor is considered to be constant.

These are assumptions that can have a heavy impact on the results. In particular, it is extremely reductive to assume that the motor operates always at the same point during its deployment. However, with the available data this assumption is necessary, in fact, in order to have more accurate results it would be necessary to collect data on the thermal aging behavior of PMs when their PC changes. To perform this type of analysis, however, requires time that is not available.

In addition, considering the constant temperature in the motor is also a limiting factor. On the one

hand, it can be assumed that when the motor operates at steady state, the temperature inside the motor stabilizes. It is also true, however, that the motor is intended to be applied in the Traction sector, and therefore its exploitation is not uniform.

In addition to the considerations made so far, it is also necessary to reflect regarding the resolution with which the study was conducted. The Torque-Speed grid of Figure 4.6 was considered during this work.

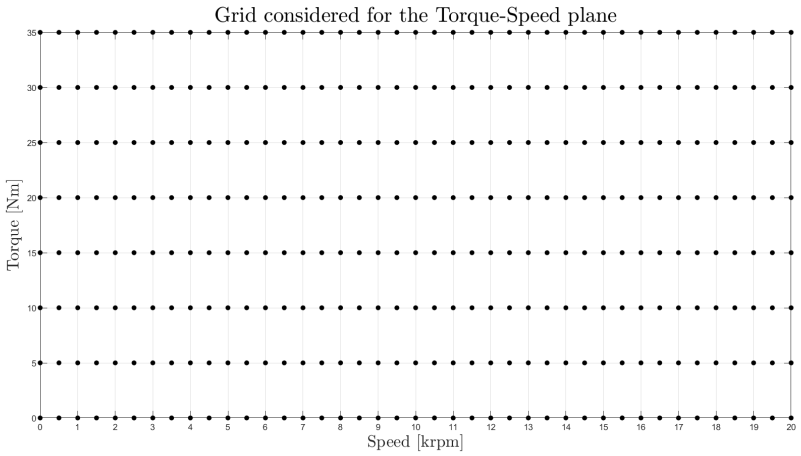

Figure 4.6: Torque-Speed grid

The resolution that was decided for the construction of the grid is mainly due to time constraints. Simulating a single point among those represented takes approximately 2 minutes, so an overly dense grid would take an inordinately long time. The grid in Figure 4.6, in the plane of currents, is as depicted in Figure 4.7. Clearly, grid resolution has an important impact on the quality of the final result. Now, keeping in mind all the considerations and assumptions made in this section, the study was conducted.

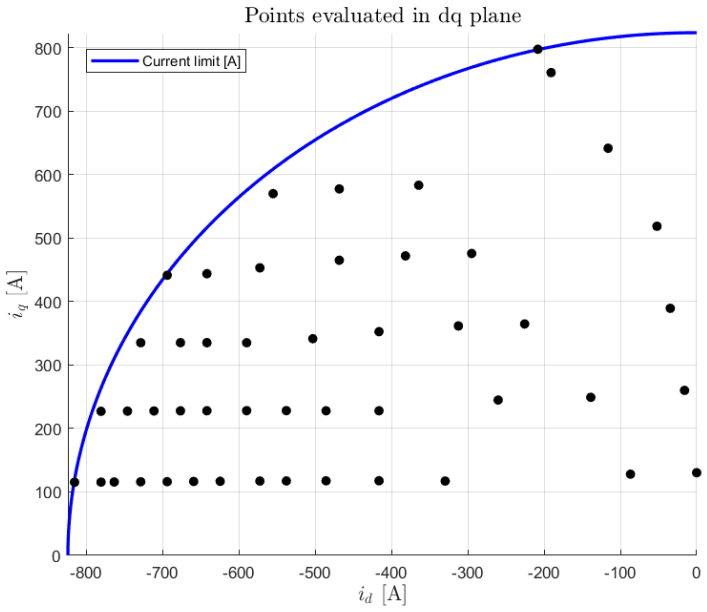

Figure 4.7: Points evaluated in the dq plane

4.2 Evaluation of the impact of aging on the IPMSM

Starting from the assumptions made in Section 4.1, it is possible to proceed with the analysis and evaluate the decay of motor performance. From the planes in Figures 4.1 and 4.2, and knowing that PC_{av} = 1.21, it was possible to derive the value of PMs remanence, B_r, under different aging times. For the analysis conducted, it was considered appropriate to know the values of B_r at 0, 10, 100, 1000, 10000 and 100000 hours of aging. Once one knows the value of B_r for a certain aging stage, one can use it in the software for FEA and obtain information regarding the performance of the motor. For each of the simulations, the analysis focused on the study of two parameters:

- The torque T [Nm]
- The efficiency η [%]

4.2.1 Torque analysis procedure

The main objective is to understand how the torque T is affected by the fact that the magnetic properties of PMs degrade. To do this, it is necessary to understand what the principle of torque generation is in an IPMSM.

They have a rotor structure such that they exhibit a marked magnetic anisotropy, as can be seen in Figure 4.3. Therefore, an IPMSM generates torque through two main mechanisms: magnetic source torque and reluctance torque. The total torque is given by the equation:

$$T = \frac{3}{2} n_{pp} \psi_m i_q + \frac{3}{2} n_{pp} (L_d - L_q) i_d i_q \tag{4.2}$$

Where n_{pp} is the number of pole pairs, ψ_m is the flux of the PMs, L_d is the direct inductance, L_q is the quadrature inductance and i_d, i_q are the direct and quadrature components of the input current.

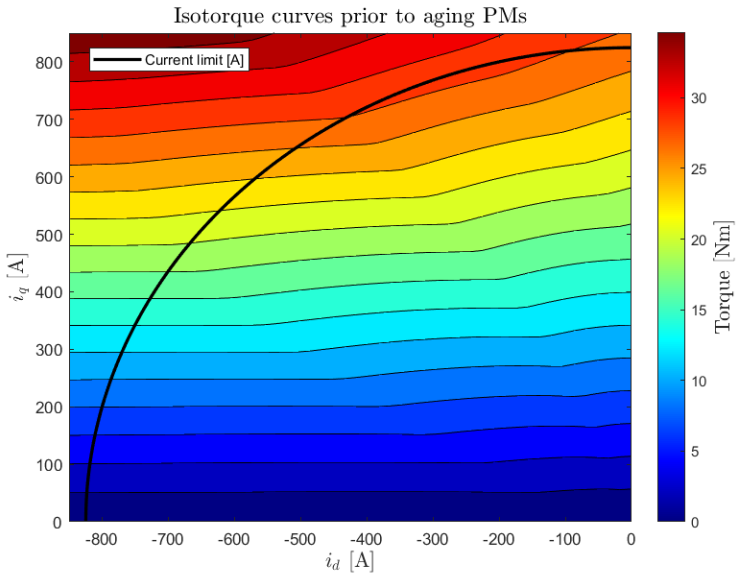

Figure 4.8: Isotorque curves before the aging of PMs

During the simulations that will be discussed in the following sections, the input current absolute value, $|I|$, was kept constant and equal to the nominal one to give a clear view of the impact that the deterioration of the magnetic properties of the PMs has on the torque. Importantly, it was assumed for the simulations that there was only one winding in each stator pit (single coil assumption).

Figure 4.8 shows the isotorque curves ($+T_n$) of the motor before any aging of the PMs. The deterioration of ψ_m affects such curves, and knowing precisely how it does so allows one to make predictions regarding the evolution of the torque as the PMs age.

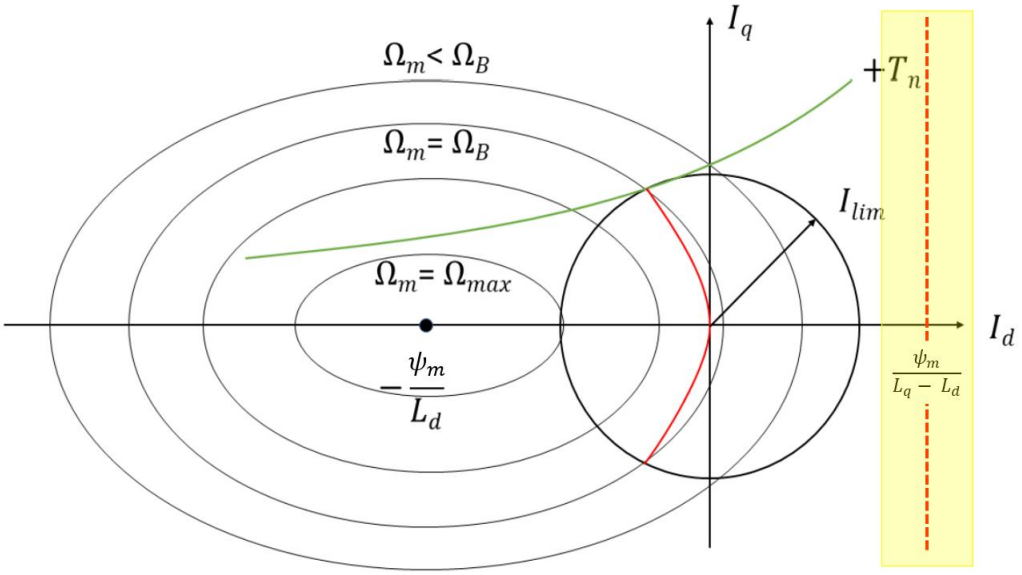

Figure 4.9: Influence of ψ_m on isotorque curves, adapted [36]

In Figure 4.9 the grey ellipses represent the isospeed curves, the green curve represents one of the isotorque curves ($+T_n$) and the continuous red lines the maximum torque per ampere line. From the figure it can be seen that the position of these curves in the plane (i_d, i_q) depends on the vertical asymptote given by the value taken by:

$$x = \frac{\psi_m}{(Lq - Ld)} \tag{4.3}$$

Since ψ_m is positive, and the difference between L_q and L_d will always be positive because of the anisotropy introduced by the motor geometry, the asymptote will always be in the first quadrant. Assuming that the denominator of Equation 4.3 remains constant over time, as the PMs age the value of ψ_m will decrease causing the value of x to move more and more toward the origin (intersection of the axis), thus affecting the isotorque curves.

It is also clear from Figure 4.9 how decreasing ψ_m affects the voltage limit, which is represented by the ellipses. In fact, due to the aging of the PMs, the center, which is given by $-\frac{\psi_m}{Ld}$, moves toward the intersection of the axis. Because of this, it is reasonable to expect that keeping constant the voltage, the motor will be able to reach a higher speed before entering the flux weakening zone.

Starting from this considerations it is possible to get an idea of how aging PMs might affect the isotorque curves, Figure 4.10 is used to indicate how the isotorque curves are expected to evolve.

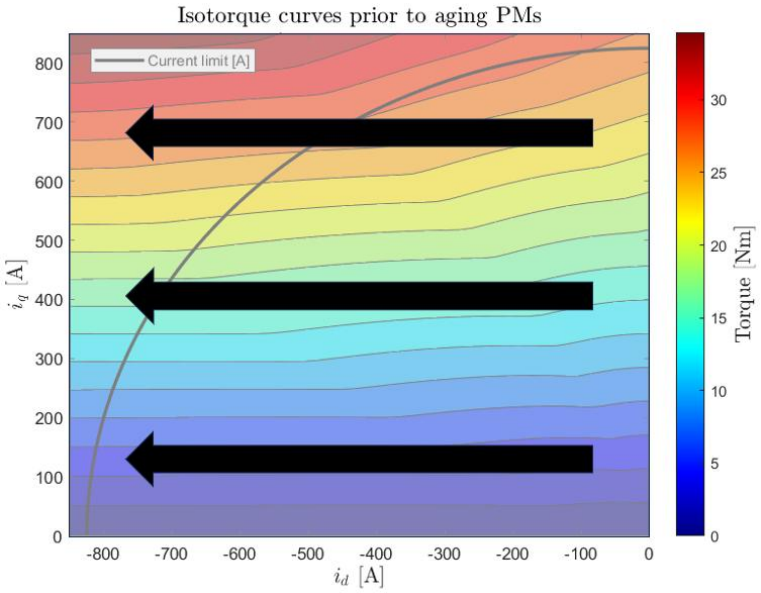

Figure 4.10: Prediction of the evolution of the isotorque curves

Thus, it is reasonable to assume that the curve representing the maximum torque that can be delivered by the motor will have a lower value than the original. Furthermore, it is expected that, while keeping the modulus of the input current, $|I|$, constant, the direct and quadrature components will undergo changes. These assumptions will be verified in the next section.

4.2.2 Efficiency analysis procedure

The other parameter that this thesis sets out to analyse is efficiency, η, as it is a term of fundamental importance from an economic and energy perspective. The goal is to understand how much and how aging PMs affect motor efficiency.

When it comes to efficiency, it is necessary to introduce the concept of losses. There are two types of losses: electric and mechanic. The electric losses are divided in three types:

- Winding losses, which are the losses due to the Joule effect in the stator windings. They are computed as follows:

$$P_{windings} = 3RI^2 \tag{4.4}$$

  where R is the electric resistance of the coils and I is the input current. Since one wants to understand, while maintaining the same input current modulus, how the aging of PMs affects efficiency, one expects this term to be constant in all phases.

- Core losses, which are given by the losses in the stator and rotor and are obtained from experimental data. They are computed as follows:

$$P_{core} = P_{stator} + P_{rotor} \tag{4.5}$$

  The core loss density was estimated with Steinmetz coefficients, obtained from experimental re-

sults during a previous work [11]. Considering a sinusoidal variation of the flux density in the rotor and stator cores, core loss density, p_{core}, is given by Equation 4.6, where f is the frequency of the flux density and B_m its amplitude, the Steinmetz coefficients k_h, k_e and k_{exc}, determined for each core material (VaCoFe and FeSi). The amplitude of flux density, was obtained from the stationary FE model, with the stator flux aligned with d and q rotor axes [11].

$$p_{core} = k_h f B_m^2 + k_e (f B_m)^2 + k_{exc} (f B_m)^{1.5} \tag{4.6}$$

- Induced currents in the PMs losses, which are the losses due to the fact that PMs, being endowed with a resistivity ρ_m = $1.3 \cdot 10^{-6}$ Ωm, are subject to induced currents. They are computed as follows:

$$P_m = \int_V \rho_m J^2 \, dV \tag{4.7}$$

  Where J is the current density of the currents induced in the PMs and the integral is made on the volume of the PMs.

Mechanical losses, on the other hand, are of two types:

- Vibration losses, which were not considered because they depend on the choice of bearings and this is not an objective of the thesis.
- Windage losses, representing the losses due to air friction in the air gap. These losses are negligible at low speeds. Since the analysis is based on motor operation at a rated speed of 7500rpm, they have therefore been neglected.

Figure 4.11 shows the motor efficiency map in the Torque-Speed plane, before aging PMs, with a maximum efficiency around 96.56% .

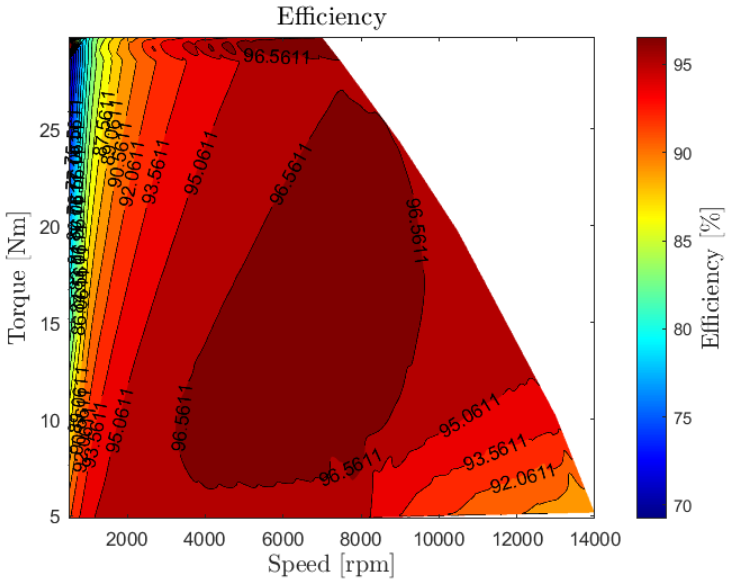

Figure 4.11: Efficiency map

4.3 Results

This section is devoted to the exposition of simulation results and their analysis. It is divided into two subsections, the former studies the variation of the torque T in time, the second the variation of the efficiency η.

4.3.1 Torque evolution

The data collected during the simulations regarding the torque study are shown in Tables 4.2 and 4.3 for the 100℃ and 120℃ tests, respectively.

Table 4.2: Important parameters during the analysis of torque evolution, 100℃

T = 100℃							
Aging time [h]	T [Nm]	T decrease [%]	B_r decrease [%]	$\|I\|$ [A]	i_d [A]	i_q [A]	PC_{av}
0	29.74	-	-	824.66	-208.16	797.96	1.21
10	29.40	1.13	1.27	822.84	-260.20	780.61	1.20
100	29.10	2.15	2.28	824.66	-312.24	763.27	1.18
1000	28.92	2.75	3.29	824.66	-312.24	763.27	1.18
10000	28.74	3.37	4.31	824.66	-312.24	763.27	1.18
100000	28.55	4.00	5.32	824.66	-312.24	763.27	1.18

Table 4.3: Important parameters during the analysis of torque evolution, 120℃

T = 120℃							
Aging time [h]	T [Nm]	T decrease [%]	B_r decrease [%]	$\|I\|$ [A]	i_d [A]	i_q [A]	PC_{av}
0	29.74	-	-	824.66	-208.16	797.96	1.21
10	29.24	1.67	1.45	824.66	-312.24	763.27	1.17
100	29.04	2.34	2.59	824.66	-312.24	763.27	1.18
1000	28.84	3.02	3.73	824.66	-312.24	763.27	1.18
10000	28.63	3.72	4.87	824.66	-312.24	763.27	1.18
100000	28.42	4.44	6.00	824.66	-312.24	763.27	1.18

A first observation concerns the value of PC_{av}, which was initially assumed to be constant during aging. It was important to verify the veracity of this assumption since, as already explained, the PC of a PM affects its aging. From Tables 4.2 and 4.3 it is observed that in 100000 hours of use the PC_{av} drops by less than 3% from the initial value, both for simulations at 100℃ and 120℃. Therefore, it can be said that the assumption is acceptable.

The torque T, as expected from the Equation 4.2, decreases due to the decay of the magnetic properties of the PMs. This occurs both following aging at 100℃ and 120℃ and is more pronounced in the latter case, as it can be seen in Figures 4.12 and 4.13, respectively. From the two Figures just mentioned, it is evident that the torque losses are less pronounced than the flux losses of PMs. The explanation is to be found in Equation 4.2.

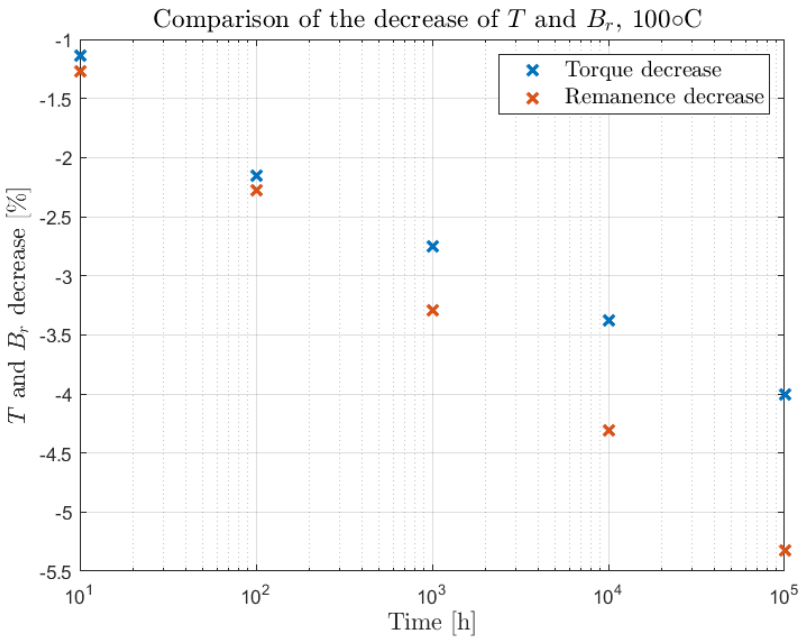

Figure 4.12: Decrease of torque and PM's remanence during a 100ºC aging

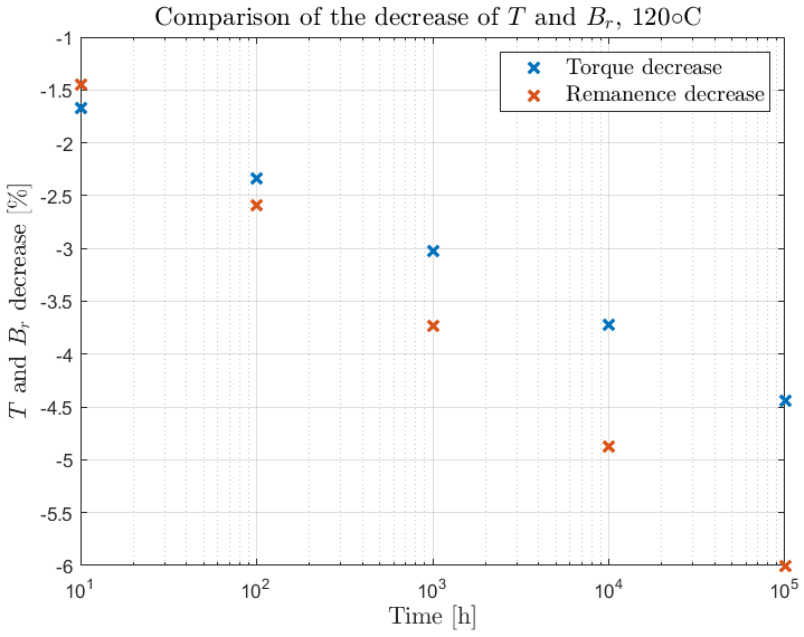

Figure 4.13: Decrease of torque and PM's remanence during a 120ºC aging

Assuming that the direct and quadrature components of the input current (i_d, i_q) remain constant, only the first term (magnetic torque) would decrease, and for this reason the rate of decrease of the flux losses of the PMs is faster than the rate of decrease of the torque losses of the motor.

Actually, as expected starting from the assumptions of Subsection 4.2.1, from Tables 4.2 and 4.3 it is observed that only the absolute value of the input current, $|I|$, remains constant and not its direct and quadrature components as shown in Figures 4.14 and 4.15 for 100 ℃ and 120 ℃, respectively.

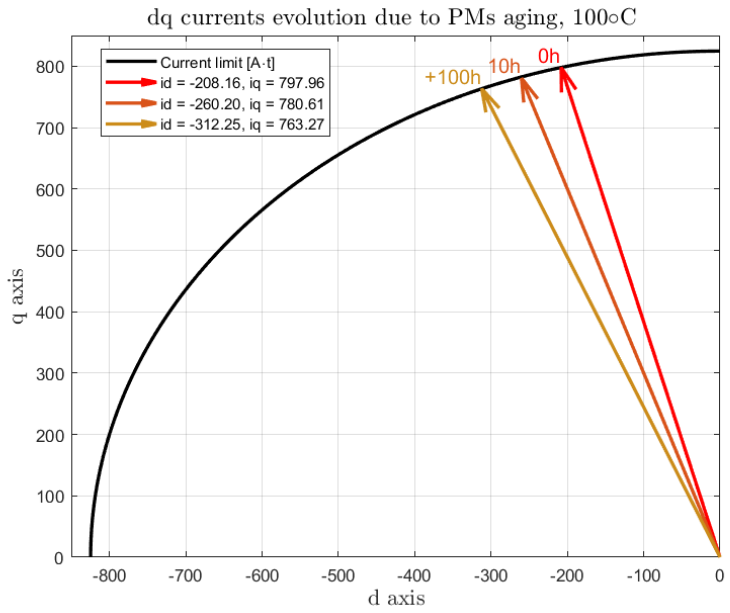

Figure 4.14: dq currents evolution over the PMs aging, 100℃

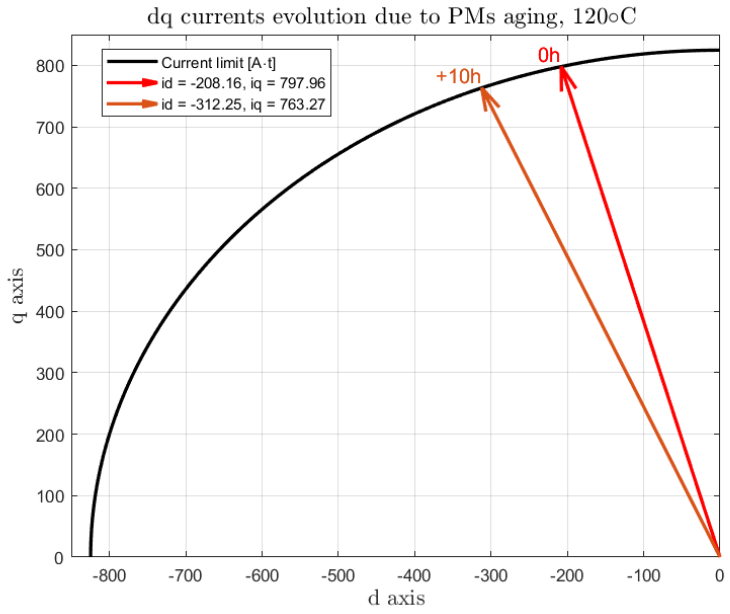

Figure 4.15: dq currents evolution over the PMs aging, 120℃

This is a relevant observation because on i_q depends the value of the magnetic torque term of Equation 4.2 and on the product $i_d i_q$ depends the value of the reluctance torque term. Thus, what happens as a result of aging PMs is that the first component decreases while the second grows trying to reach the nominal torque value established in the first simulation.

A final consideration concerns the fact that after a certain aging stage of PMs the pair (i_d, i_q) stabilizes at a constant value. This is probably due to the level of accuracy of the grid as discussed in Section 4.1, in particular observe Figure 4.7.

4.3.2 Efficiency evolution

The second objective of the simulations is to determine how the decay of PMs properties is related to the efficiency, η, of the motor. The efficiency calculation, for the i-th aging stage, is as follows:

$$\eta_i = (1 - \frac{\text{total losses}_i}{T_i \cdot \omega}) \cdot 100 \tag{4.8}$$

Considering the losses mentioned in Subsection 4.2.2, the new equation becomes:

$$\eta_i = (1 - \frac{P_{windings_i}\text{-}P_{core_i}\text{-}P_{m_i}}{T_i \cdot \omega}) \cdot 100 \tag{4.9}$$

Where ω represents the speed (remember that only the point of operation at nominal speed is analyzed) expressed in [rad/s].The data collected regarding machine efficiency are shown in Tables 4.4 and 4.5.

Table 4.4: Evolution of efficiency over time, 100℃

T = 100℃		
Aging time [h]	B_r decrease [%]	η [%]
0	-	96.09
10	1.27	96.05
100	2.28	95.98
1000	3.29	95.96
10000	4.31	95.93
100000	5.32	95.91

Table 4.5: Evolution of efficiency over time, 120℃

T = 120℃		
Aging time [h]	B_r decrease [%]	η [%]
0	-	96.09
10	1.45	96.01
100	2.59	95.98
1000	3.73	95.95
10000	4.87	95.92
100000	6.00	95.89

It can be seen from both Tables that efficiency, while decreasing, does not do so appreciably. This indicates that the aging of PMs does not lead to a decrease in motor efficiency and is positive in energy terms. The reasons behind this phenomenon are to be found in the impact that each loss considered has on the total losses. For this reason, for both 100℃ and 120℃ simulations, Tables 4.6 and 4.7 were created to provide a summary.

Table 4.6: Impact of each loss, 100℃

T = 100℃				
Aging time [h]	$P_{windings}$ [W]	P_{core} [W]	P_m [W]	total [W]
0	731	118	38	887
10	728	126	48	902
100	732	120	55	907
1000	732	119	56	907
10000	732	119	57	908
100000	732	118	59	909

Table 4.7: Impact of each loss, 120℃

T = 120℃				
Aging time [h]	$P_{windings}$ [W]	P_{core} [W]	P_m [W]	total [W]
0	731	118	38	887
10	732	121	54	907
100	732	120	56	908
1000	732	119	57	908
10000	732	118	58	908
100000	732	117	59	909

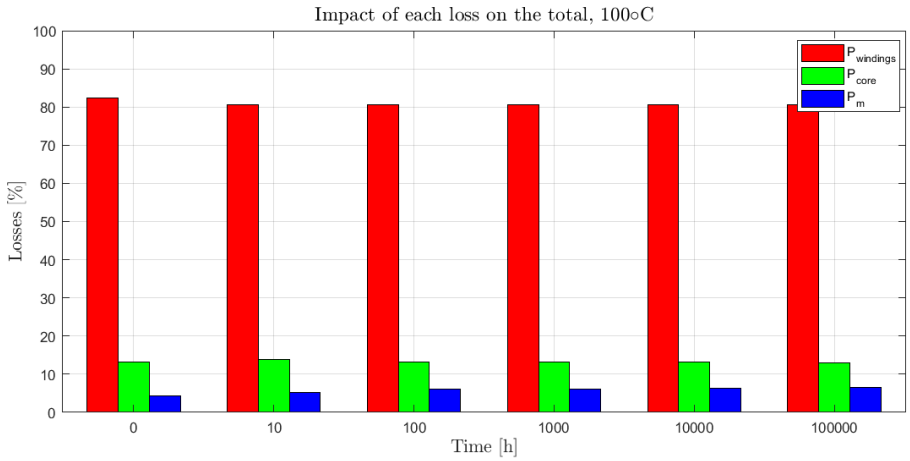

Figure 4.16: Impact of each loss for simulations at 100℃

As expected the $P_{windings}$ are constant since they are proportional to $|I|^2$, which does never change. Only in the simulation after 10h at 100℃ is a slightly different value observed. This is due to the fact that, during that simulation, due to the reduced grid resolution, the modulus of the input current was slightly smaller than in the other simulations (see Table 4.2). The winding losses account for about 80% of total, making them the largest factor in motor losses, as shown in Figure 4.16, which refers to the results obtained during simulations at 100℃. For simulations at 120℃, almost identical results were obtained. The P_{core} have a slightly unexpected behavior, in fact, they were expected to decrease as the PMs age. This is true except for an initial instant in which they appear to grow in both the 100℃

and 120℃ simulations. However, there is a need to consider that these losses are subject to numerical errors and this is where the cause may lie. These losses are about 13% of the total losses during the whole aging period. However, total losses increase, albeit marginally, due to the fact that losses due to induced currents established in PMs, P_m increase. These depend on the value of i_d. It was previously observed that aging of PMs causes the i_d and i_q components of the input current to vary. During use, it is observed that i_d increases (in absolute value) and that is why P_m increases as Figure 4.17 shows. Then from Table 4.8 it is possible to study the relation between the increase of the component i_d (in absolute value) and the increase of P_m.

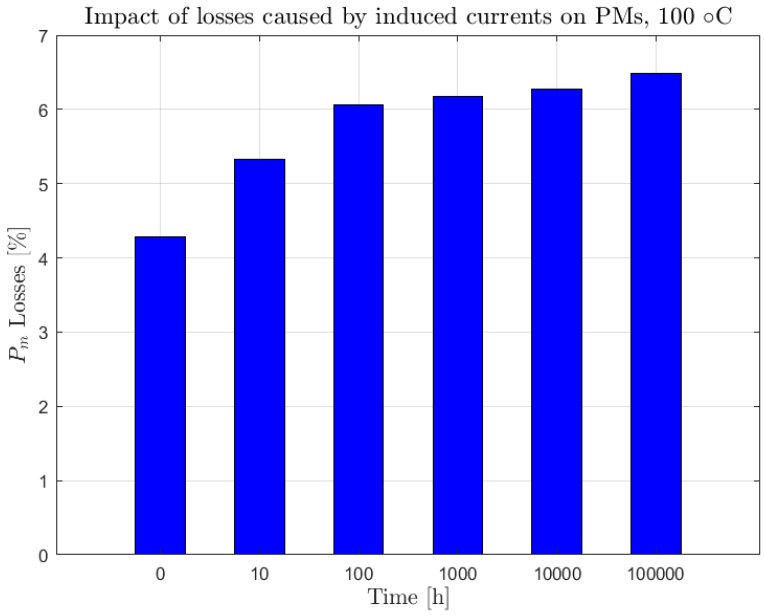

Figure 4.17: Zoom on the impact of P_m losses

Table 4.8: Relation between i_d and impact of P_m on total losses, 100℃

T = 100℃				
Aging time [h]	i_d [A]	P_m [%]	$\|i_d\|$ increase [%]	P_m increase [%]
0	-208.16	4.33	-	-
10	-260.20	5.36	25	24
100	-312.24	6.08	50	40
1000	-312.24	6.23	50	44
10000	-312.24	6.28	50	45
100000	-312.24	6.45	50	50

In this table, the column "$|i_d|$ increase [%]" refers to how much i_d increases as a percentage from the starting value of -208.16A and the same concept applies for "P_m increase [%]". These parameters are crucial to understand the relation between i_d and P_m. The table shows how the increase in modulus of i_d is approximately proportional to the growth of P_m. However, since the latter have an almost marginal effect on total losses, an increase of more than 100A in i_d causes P_m to increase only from 4% to 6.5% of total losses. This means that their final impact can be considered almost unchanged compared to

during the entire period of motor use.

As a result of this consideration, it is then explained why the efficiency of the motor, shown in Table 4.4 appears to hardly decrease throughout the aging period of the motor.

Chapter 5

Conclusions

The objective of this thesis work was to determine how aging of permanent magnets (PMs), as a result of their exposure to high temperatures, affects the performance of the electric motor in which they are applied.

To reach this conclusion, the thesis was structured in two parts: an initial experimental part was devoted to data acquisition by conducting aging tests. In order to do this, it was first necessary to construct a framework for measuring the magnetic flux density, B, of PMs. This structure had to meet two requirements: accuracy and low cost of creation. Once the method devised was validated, it was applied for experimental data acquisition.

At this stage, the magnets were placed, for increasing times, inside an oven at a temperature of 140 ℃. Three samples of BMN-42SH, operating at three different PCs, were tested simultaneously to define how the working point of a magnet affects its aging. For all three samples, the results showed almost no decay in magnetic properties. At this point it was hypothesized that the temperature of the environment might affect the BH curve of the PMs more than the datasheet indicated, thus distorting the measurements. Therefore, it was decided to conduct a study regarding the influence of the ambient temperature, which confirmed what was reported in the datasheet. Then, since there was no certainty regarding the origin of the PMs, it was hypothesized that they may have already been in an advanced state of aging before the oven tests began. To validate this theory, an additional 200-hour oven cycle was introduced for just one of the samples, which again showed almost no decay in magnetic properties. This result seemed to lend credence to the theory that the magnets tested were already in an aging state when the tests began. For further verification, it was decided to repeat the same thermal cycle performed for the BMN-42SH samples, for a BMN-48SH sample. For the latter, it was certain that it was not at an advanced aging stage. However, these tests also showed that the magnet was not aging. These results, although justifiable by the quality of the measurements, are at odds with the literature and for this reason, it was decided to use the data previously obtained from a colleague [11] to move on to the second part of the thesis.

This part focused on applying this data to define what impact the aging of magnets has on the performance of the electric motor. The data collected was up to 186 hours of aging at temperatures of

100℃ and 120℃. Since this is a limited number of hours, an adaptation of the Arrhenius model was applied to obtain a prediction of aging for longer times, up to 100000 hours. In order to assess how motor performance changed as the PMs aged, it was decided to evaluate torque and efficiency for the same machine operating point (same torque and speed). During the analysis, the input current modulus was kept constant in order to obtain comparable results.

With regard to the evolution of torque over time, it was observed that it decreases due to the decay of the magnetic properties of the PMs, as was to be expected. The rate of torque decay is less than that of the magnetic properties of the magnets. It has also been observed that the value of ψ_m influences the position of the isotorque curves in the plane (i_d, i_q). Therefore, while keeping the modulus of the input current constant, the operating point (i_d, i_q) changes slightly as a result of the decay of ψ_m.

With regard to the analysis of the evolution of efficiency over time, it was observed that the impact of the aging of the PMs is negligible and the reason for this is to be found in the distribution of motor losses. The winding losses during the entire aging process accounted for approximately 80% of the total losses. Losses in the core, on the other hand, decreased slightly, as to be expected, but was almost negligible. These losses accounted for about 13% during the entire aging period. The only losses that increased were those due to the induced currents in the PMs, but this growth had an almost negligible impact on the final result because these were the least significant losses. In fact, they increased from 4% to 6% of the total losses during aging. It is for these reasons that the efficiency of the engine, despite aging PMs, remains almost constant.

5.1 Achievements

The work presented in this thesis is only the introduction to a work that will have to expand over time in order to obtain more precise and significant results. However, during these months a number of results have been obtained that can be used by future colleagues to continue what has been started. A list of the main objectives achieved is as follows:

- An accurate and inexpensive method for measuring the average magnetic flux density $\langle B_m \rangle$ of PMs has been developed.

- It has been verified that the temperature of the environment in which the measurements are taken is indeed what is indicated on the datasheet.

- By adapting the Arrhenius model, it was possible to obtain an estimate of the aging of PMs over a large number of hours at a certain temperature of use.

- Using finite element analysis (FEA), a study was performed on the evolution of torque and motor efficiency following the decay of the magnetic properties of PMs.

5.2 Future Work

For the continuation of this work, the first step will certainly be to understand exactly how PMs age. Indeed, the data obtained in this thesis, although justified, is at odds with the literature. This raises the interest in carrying out further tests in an oven, perhaps by applying a different method for measuring the magnetic flux density.

Once this problem is solved, the next step may be to perform aging tests at a non-constant temperature, as it is limiting to consider that the electric motor in which the PMs are applied always works at the same temperature. In this way, during future FEA simulations, it will be possible to improve the accuracy of the results obtained in this thesis regarding torque and efficiency decay.

Finally, in this thesis, it was considered that during the entire aging cycle (100,000h), the motor would always work at the same torque-speed point, causing the PC of the PMs to be constant. Obviously, this is a major limitation, especially considering that one is dealing with a motor for traction applications. Therefore, a further challenge will be to understand how the variation of the PC during use affects the aging of the PMs and consequently the performance of the motor.

Bibliography

[1] X. Duan, X. Zhang, Y. Tang, and M. Hao. Cogging torque reduction in pmsm in wide temperature range by response surface methodology. *Symmetry*, 13(10), 2021. ISSN 2073-8994. doi: 10.3390/sym13101877.

[2] K. L. Yang and Q. Song. Study on influencing factors on reliability of permanent magnet synchronous motor system in electric vehicle. In *Advances in Product Development and Reliability III*, volume 544 of *Advanced Materials Research*, pages 151–158. Trans Tech Publications Ltd, 9 2012. doi: 10.4028/www.scientific.net/AMR.544.151.

[3] D.-W. Kim, D. H. Kang, C.-H. Kim, J.-S. Kim, Y.-J. Kim, and S.-Y. Jung. Operation characteristic of ipmsm considering pm saturation temperature. *IEEE Transactions on Applied Superconductivity*, 30(4):pages 1–4, 2020. doi: 10.1109/TASC.2020.2989799.

[4] J. Lee, K. Nam, S. Choi, and S. Kwon. Loss minimizing control of pmsm with the use of polynomial approximations. In *2008 IEEE Industry Applications Society Annual Meeting*, pages 1–9, 2008. doi: 10.1109/08IAS.2008.226.

[5] D. Fernández, M. Martinez, D. Reigosa, J. M. Guerrero, C. M. S. Alvarez, and F. Briz. Permanent magnets aging in variable flux permanent magnet synchronous machines. *IEEE Transactions on Industry Applications*, 56(3):pages 2462–2471, 2020.

[6] W. Tong, R. Sun, C. Zhang, S. Wu, and R. Tang. Loss and thermal analysis of a high-speed surface-mounted pmsm with amorphous metal stator core and titanium alloy rotor sleeve. *IEEE Transactions on Magnetics*, 55(6):pages 1–4, 2019. doi: 10.1109/TMAG.2019.2897141.

[7] G. Pellegrino and F. Cupertino. Fea-based multi-objective optimization of ipm motor design including rotor losses. In *2010 IEEE Energy Conversion Congress and Exposition*, pages 3659–3666, 2010. doi: 10.1109/ECCE.2010.5618310.

[8] D. F. Alonso, C. Suarez, J. Guerrero, and F. Briz. Impact of machine magnetization state on permanent magnet losses in permanent magnet synchronous machines. In *2017 IEEE Energy Conversion Congress and Exposition (ECCE)*, pages 5840–5845. IEEE, 2017.

[9] L. Bernard and L. Daniel. Effect of stress on magnetic hysteresis losses in a switched reluctance motor: Application to stator and rotor shrink fitting. *IEEE Transactions on Magnetics*, 51(9):pages 1–13, 2015. doi: 10.1109/TMAG.2015.2435701.

[10] A. S. Nunes, L. Daniel, M. Hage-Hassan, and M. Domenjoud. Modeling of the magnetic behavior of permanent magnets including ageing effects. *Journal of Magnetism and Magnetic Materials*, 512: pages 166930, 2020. ISSN 0304-8853. doi: https://doi.org/10.1016/j.jmmm.2020.166930.

[11] P. P. C. Bhagubai, L. F. D. Bucho, J. F. P. Fernandes, and P. J. Costa Branco. Optimal design of an interior permanent magnet synchronous motor with cobalt iron core. *Energies*, 15(8), 2022. ISSN 1996-1073. doi: 10.3390/en15082882.

[12] P. P. C. Bhagubai, J. G. Sarrico, J. F. P. Fernandes, and P. J. Costa Branco. Design, multi-objective optimization, and prototyping of a 20 kw 8000 rpm permanent magnet synchronous motor for a competition electric vehicle. *Energies*, 13(10), 2020. ISSN 1996-1073. doi: 10.3390/en13102465.

[13] R. Mocanu and A. Onea. Phase resistance estimation and monitoring of pmsm used in electrical vehicles. In *2014 18th International Conference on System Theory, Control and Computing (ICSTCC)*, pages 512–519. IEEE, 2014.

[14] J. Pyrhönen, J. Nerg, P. Kurronen, J. Puranen, and M. Haavisto. Permanent magnet technology in wind power generators. In *The XIX International Conference on Electrical Machines - ICEM 2010*, pages 1–6, 2010. doi: 10.1109/ICELMACH.2010.5608312.

[15] M. Chinchilla, S. Arnaltes, and J. Burgos. Control of permanent-magnet generators applied to variable-speed wind-energy systems connected to the grid. *IEEE Transactions on Energy Conversion*, 21(1):pages 130–135, 2006. doi: 10.1109/TEC.2005.853735.

[16] B. Hongpeechar, W. Krueasuk, A. Poungching-ngam, P. Bhasaputra, and W. Pattaraprakorn. Feasibility study of micro hydro power plant for rural electrification in thailand by using axial flux permanent magnet. In *2011 International Conference Utility Exhibition on Power and Energy Systems: Issues and Prospects for Asia (ICUE)*, pages 1–4, 2011. doi: 10.1109/ICUEPES.2011.6497732.

[17] P. König, D. Sharma, K. R. Konda, T. Xie, and K. Höschler. Comprehensive review on cooling of permanent magnet synchronous motors and their qualitative assessment for aerospace applications. *Energies*, 16(22), 2023. ISSN 1996-1073. doi: 10.3390/en16227524.

[18] A. Schramm and D. Gerling. Researches on the suitability of switched reluctance machines and permanent magnet machines for specific aerospace applications demanding fault tolerance. In *International Symposium on Power Electronics, Electrical Drives, Automation and Motion, 2006. SPEEDAM 2006.*, pages 56–60, 2006. doi: 10.1109/SPEEDAM.2006.1649744.

[19] J. Ormerod. Permanent magnet markets and applications. In *Modern Permanent Magnets*, pages 403–434. Elsevier, 2022.

[20] T. Haring, K. Forman, T. Huhtanen, and M. Zawadzki. Direct drive-opening a new era in many applications. pages 171–179, 2003.

[21] T. Vaimann, A. Kallaste, A. Kilk, and A. Belahcen. Magnetic properties of reduced dy ndfeb permanent magnets and their usage in electrical machines. In *2013 Africon*, pages 1–5. IEEE, 2013.

[22] R. Sami. Demagnetisation of permanent magnets in electrical machines. *OH presentation, Helsinki University*, 2006.

[23] S. J. Rind, Y. Ren, Y. Hu, J. Wang, and L. Jiang. Configurations and control of traction motors for electric vehicles: A review. *Chinese Journal of Electrical Engineering*, 3(3):pages 1–17, 2017. doi: 10.23919/CJEE.2017.8250419.

[24] A. M. El-Refaie. Motors/generators for traction/propulsion applications: A review. *IEEE Vehicular Technology Magazine*, 8(1):pages 90–99, 2013.

[25] M. L. De Klerk and A. K. Saha. A comprehensive review of advanced traction motor control techniques suitable for electric vehicle applications. *IEEE Access*, 9:pages 125080–125108, 2021.

[26] V. P. Melo, P. P. C. Bhagubai, J. F. P. Fernandes, and P. J. Costa Branco. Impact of permanent magnet aging on the performance of synchronous motors for traction applications. In *2023 IEEE International Conference on Environment and Electrical Engineering and 2023 IEEE Industrial and Commercial Power Systems Europe (EEEIC / ICPS Europe)*, pages 1–6, 2023. doi: 10.1109/EEEIC/ICPSEurope57605.2023.10194809.

[27] M. Haavisto, S. Tuominen, H. Kankaanpää, and M. Paju. Time dependence of demagnetization and flux losses occurring in sintered nd-fe-b permanent magnets. *IEEE Transactions on Magnetics*, 46 (9):pages 3582–3584, 2010.

[28] M. Haavisto, H. Kankaanpää, and M. Paju. Estimation of time-dependent polarization losses in sintered nd-fe-b permanent magnets. *IEEE transactions on Magnetics*, 47(1):pages 170–174, 2010.

[29] M. Haavisto, H. Kankaanpää, and M. Paju. Estimation of time-dependent polarization losses in sintered nd-fe-b permanent magnets. *IEEE Transactions on Magnetics*, 47(1):pages 170–174, 2011. doi: 10.1109/TMAG.2010.2089692.

[30] S. Möwius, N. Kropff, and M. Velicescu. Measurement technologies for permanent magnets. *ACTA IMEKO*, 7(4):pages 15–20, 2018.

[31] R. Allcock and S. Constantinides. Magnetic measuring techniques for both magnets and assemblies. *Arnold Magnetic Technologies: Rochester, NY, USA*, 2012.

[32] M. Haavisto and M. Paju. Temperature stability and flux losses over time in sintered nd–fe–b permanent magnets. *IEEE Transactions on Magnetics*, 45(12):pages 5277–5280, 2009. doi: 10.1109/TMAG.2009.2023907.

[33] M. Haavisto, S. Tuominen, T. Santa-Nokki, H. Kankaanpää, M. Paju, P. Ruuskanen, et al. Magnetic behavior of sintered ndfeb magnets on a long-term timescale. *Advances in Materials Science and Engineering*, 2014, 2014.

[34] O. Bilgin and F. A. Kazan. The effect of magnet temperature on speed, current and torque in pmsms. In *2016 XXII International Conference on Electrical Machines (ICEM)*, pages 2080–2085, 2016. doi: 10.1109/ICELMACH.2016.7732809.

[35] URL https://www.associatedenvironmentalsystems.com/products/BHD-202.

[36] A. Gays. *Calcolo analitico della coppia elettromagnetica di macchine sincrone IPM V-shape= Analytical calculation of the electromagnetic torque of V-shape IPM synchronous machines*. PhD thesis, Politecnico di Torino, 2019.

Appendix A

BMN-42SH Datasheet

BOMATEC
MORE THAN JUST MAGNETS

BMN-42SH NdFeB sintered

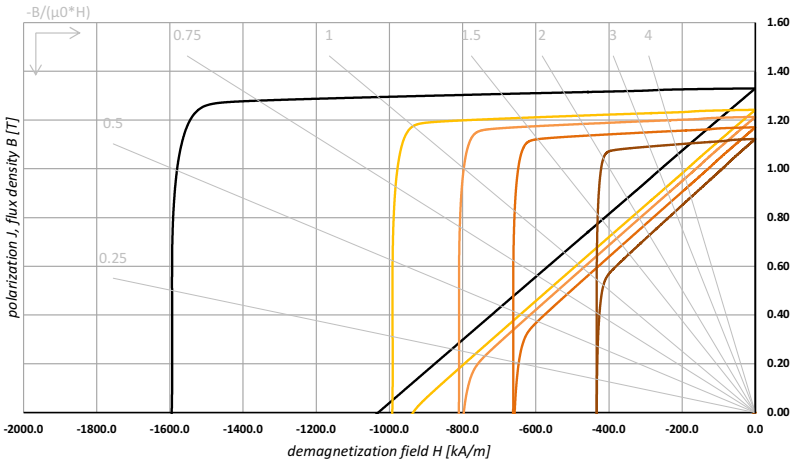

Temperature in [°C]:		20.0	80.0	100.0	120.0	150.0	
magnetic properties							
Remanence 20°C	Br min	1.290	T	12.9	kG		
	Br nom	1.330	T	13.3	kG		
Coercitivity 20°C	HcB min	976	kA/m	12.3	kOe		
	HcB nom	1018	kA/m	12.8	kOe		
Intrinsic Coercitivity 20°C	HcJ min	1592	kA/m	20.0	kOe		
	HcJ nom	1595	kA/m	20.0	kOe		
Maximum Energy Product 20°C	BH max, min	318	kJ/m^3	39.9	MGOe		
	BH max, nom	334	kJ/m^3	42.0	MGOe		
Reversible Temperature Coefficient [1]	α Br nom	-0.100 ~ -0.120	%/°C				
	β HcJ nom	-0.55 ~ -0.66	%/°C				
material properties (typical values)							
Max. Operating Temperature [2]	T max	150	°C				
Density	ρ	7.55	g/cm^3				
Permeability 20°C	μr	1.05					
Vickers Hardness		500 - 600	HV				
Modulus of Elasticity	E	150 - 200	kN/mm^2				
Copressive Strength		1000 - 1100	N/mm^2				
Flexural Strength		250	N/mm^2				
Expansion Coefficient		-	$10^{-6}/K$				
Expansion Coefficient in direction of	⊥	-3 - 0	$10^{-6}/K$				
anisotropy	//	4 - 9	$10^{-6}/K$				
Specific Electric Resistance	ρel	1.2 - 1.6	μΩ·m				
Specific Heat Capacity	c	440	J/(kg·K)				
Thermal Conductivity	λ	8.0 - 10.0	W/m·K				

1) The shown temperature coefficients are nominal reference values only . They can vary for different temperatures and don't need to be linear.

2) The maximum operating temperature is depending on the magnet shape, size and on the specific application.

Note: The above plotted graphs are idealized and represent theoretical values of the material. Shown are curves according nominal values based on uncoated material samples according to IEC 60404-5. Material and magnetic data represent typical data that may vary due to product shape, size and coating. Please contact Bomatec regarding specific requirements for your application.

Bomatec |Hofstrasse 1 |Tel. +41 44 872 10 00 |Fax. +41 44 872 10 01 |contact@bomatec.ch | www.bomatec.com

Appendix B

BMN-48SH Datasheet

BOMATEC
MORE THAN JUST MAGNETS

BMN-48SH/S (GBD) NdFeB sintered, corrosion stable

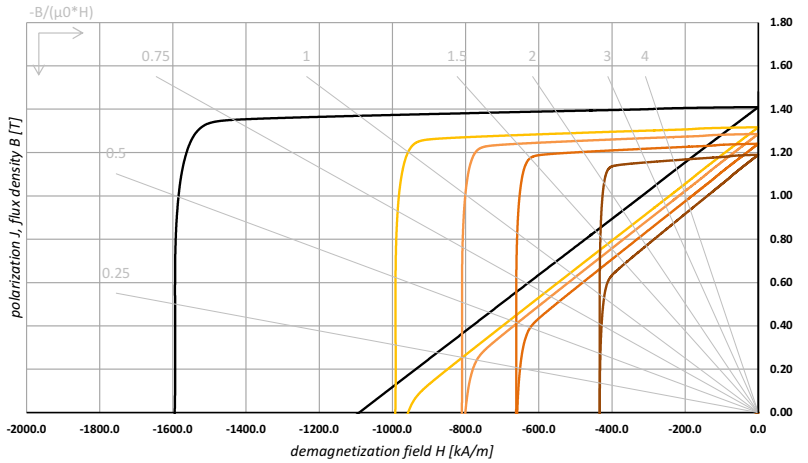

Temperature in [°C]:		20.0	80.0	100.0	120.0	150.0	
magnetic properties							
Remanence 20°C	Br min	1.370	T	13.7	kG		
	Br nom	1.410	T	14.1	kG		
Coercitivity 20°C	HcB min	1024	kA/m	12.9	kOe		
	HcB nom	1074	kA/m	13.5	kOe		
Intrinsic Coercitivity 20°C	HcJ min	1592	kA/m	20.0	kOe		
	HcJ nom	1595	kA/m	20.0	kOe		
Maximum Energy Product 20°C	BH max, min	358	kJ/m^3	45.0	MGOe		
	BH max, nom	382	kJ/m^3	48.0	MGOe		
Reversible Temperature Coefficient [1]	α Br nom	-0.100 ~ -0.120	%/°C				
	β HcJ nom	-0.55 ~ -0.66	%/°C				
material properties (typical values)							
Max. Operating Temperature [2]	T max	150	°C				
Density	ρ	7.55	g/cm^3				
Permeability 20°C	μr	1.05					
Vickers Hardness		500 - 600	HV				
Modulus of Elasticity	E	150 - 200	kN/mm^2				
Copressive Strength		1000 - 1100	N/mm^2				
Flexural Strength		250	N/mm^2				
Expansion Coefficient		-	$10^{-6}/K$				
Expansion Coefficient in direction of	⊥	-3 - 0	$10^{-6}/K$				
anisotropy	//	4 - 9	$10^{-6}/K$				
Specific Electric Resistance	ρel	1.2 - 1.6	μΩ·m				
Specific Heat Capacity	c	440	J/(kg·K)				
Thermal Conductivity	λ	8.0 - 10.0	W/m·K				

1) The shown temperature coefficients are nominal reference values only . They can vary for different temperatures and don't need to be linear.

2) The maximum operating temperature is depending on the magnet shape, size and on the specific application.

Note: The above plotted graphs are idealized and represent theoretical values of the material. Shown are curves according nominal values based on uncoated material samples according to IEC 60404-5. Material and magnetic data represent typical data that may vary due to product shape, size and coating. Please contact Bomatec regarding specific requirements for your application.

Bomatec |Hofstrasse 1 |Tel. +41 44 872 10 00 |Fax. +41 44 872 10 01 |contact@bomatec.ch | www.bomatec.com

Appendix C

Gaussmeter

HIRST Magnetic Instruments Ltd.

SPECIFICATIONS

Model	GM08 and GM07
SI Units	0.000 - ±3.000 Tesla (00.00 - ±30.00 kiloGauss) 000.0 - ±299.9 milliTesla (0.000 - ±2.999 kiloGauss) 00.00 - ±29.99 milliTesla (000.0 - ±299.9 kiloGauss) 00.00 - ±2.999 milliTesla (00.00 - ±29.99 kiloGauss)
Units of measurement	Tesla, Gauss, Amps/m or Oersted
Frequency Range	DC and 15 Hz to 10 kHz
Functions	DC,DC peak, AC RMS, AC PEAK, AC MAX
DC Accuracy	Better than +/- 0.5% Probe and Gaussmeter max calibrated against an NMR Teslameter NPL Traceable ±1% Probe and Gaussmeter
Reproducibility	Better than ±0.5%
Display	Back lit +/- 7 digit, dedicated, transflective LCD display.
Internal memory	Non-volatile storage of gaussmeter settings
Temperature coefficient	Better than ±0.1 % of reading/°C including probe
Battery Type	4 x AA cells Long-life 1,5V Alkaline
USB and RS232	Used for data transfer and remote control. Software handshaking. USB 1.1 Compliant
Analogue Output	+/-3 Volts full scale
Time keeping	Stored data is time stamped
External PSU Socket	Included –5/6V (100-500mA)
PC Software	Windows communication software
Temperature	
- utilisation	0°C - 50°C (30°F + 125°F)
- Stockage	20°C - 70°C (70°F + 150°F)
Dimensions:	
- Length	175 mm (6.9 in)
- Width	89 mm (3.5 in)
- Height	40 mm (1;6 in)
Weight:	
(Exluding batteries)	430 g (15 oz)

GM08 Only

What you get:

GM08 Includes:

- GM08 Gaussmeter
- Transverse Probe
- Calibration Certificate
- Zero Flux Chamber
- USB lead
- Plastic carrying case

GM07 Includes:

- GM07 Gaussmeter
- Transverse Probe
- Calibration Certificate
- Zero Flux Chamber
- Plastic carrying case

CALIBRATION

A calibration certificate, traceable to NPL (National Physical Laboratory – UK NIM) standards, is supplied with the unit. Annual calibration is supported.

Hirst Magnetic Instruments Ltd. is a company with more than 60 years of experience in magnetic measurement, manufacture, install, service and calibrate a wide range of magnetic instruments and magnetic equipment. As well as Gaussmeters, Hirst also offers Integrating Fluxmeters, Pulsed Field Magnetometers (PFMs), magnetisers, magnet calibrators, demagnetisers . In addition to standard equipment, the Hirst designs incorporate a flexible architecture, offering the simple implementation of dedicated, bespoke systems for all application.

MAGNETIC SYSTEMS FOR SCIENCE AND INDUSTRY

HIRST MAGNETIC INSTRUMENTS LTD.
Tesla House,Tregoniggie Ind. Estate
Falmouth, Cornwall, TR11 4SN, U.K.
T: +44 (0) 1326 372734 e: sales@hirst-magnetics.com
w: www.gaussmeter.co.uk

Appendix D

OV301 oven

easycomposites
share the knowledge

PRECISION BENCHTOP CURING OVEN

OV301

Key Features

- Precision temperature control
- Ambient to 200°C / 392°F
- Programmable ramp and soak
- Two independent vacuum ports
- Very high thermal efficiency
- Powerful 2kW heating power
- Fan assisted forced convection
- Rugged build for production use

"Unrivalled value for money along with incredible features and performance put OV301 in a league of its own"

Designed, manufactured and quality assured in-house by Easy Composites Ltd in the UK, OV301 is a fully featured programmable industrial curing oven for convenient bench-top installation.

The oven is particularly suited for composites use, including curing or post-curing laminates, prepregs, thermoplastics, castings and moulds.

The precision manufactured, sturdy design is engineered for demanding everyday production use whilst the convenient bench-top size and precision control makes the oven equally suited to laboratory or R&D use.

OV301 has been meticulously designed to offer unrivalled thermal efficiency meaning that complete prepreg curing cycles can be completed for only a few pence*.

Recommended For:

- Curing of prepreg composite parts
- Post-curing of high temperature moulds and tooling
- Curing thermoplastics such as PP and PLA
- Curing silicones and casting resins
- Research and development/material testing

*2hr cure cycle, 20°C ambient, 1.5kwh @£0.15/kWh, total cost £0.20

Precision Temperature Control with Ramp and Soak/Dwell Functionality

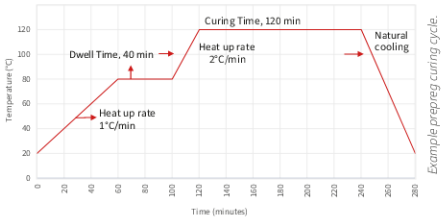

Example prepreg curing cycle.

The oven delivers the highest standards of PID temperature control accuracy, utilising high-quality calibrated thermocouple temperature measurement coupled with effective fan-assisted airflow to minimise stratification.

OV301 includes full 'ramp and soak' temperature control which can control heating rates (degrees per minute), and hold for a specific length of time at set temperatures. Although useful in a range of curing processes, 'ramp and soak' control like this is a feature usually reserved for advanced laboratory ovens and autoclaves.

Temperature, ramp and soak are all fully programmable so recommended cure and post-cure cycles for different materials can be saved and run automatically for the ultimate in precision and consistency.

OV301 - PRECISION BENCHTOP CURING OVEN

Options

OV301 has been designed from the ground-up to offer all the functionality desirable in a fully-featured composites curing oven and as such is available with a choice of options to ensure it provides a 'turn-key' system to match your needs.

USB Programming Module

OV301's fully featured PID controller is programmable with up to 8 discreet programs, each with up to 8 individual steps. Programs can be configured on the controller itself but for maximum ease-of-use, an optional USB Programming Module can be connected to the oven's communication socket for convenient programming & monitoring.

Requires Windows® PC or laptop computer, not included.

Vacuum Valve/Gauge Assemblies

OV301 includes two integral ports which can be supplied complete with optional gauge and valve assemblies for convenient connection of one or two separate vacuum lines into the oven.

Photo shows two optional vacuum valves fitted.

Additional Shelf

The OV301 Precision Composites Curing Oven is supplied with one internal shelf as standard. Adding an additional shelf can provide more flexibility when loading, particularly when loading smaller items.

Spare Parts

A full set of spare parts is available for the oven from stock, including replacement door seal, fan, heating element and the complete control and power assembly. Please contact sales for pricing.

Specification

Mains Power	230V/50Hz	
Max. Oven Temperature	200°C (392°F)	
Max. Power Consumption	2.2kW	
Maximum Current	12.5 Amps	
Internal Capacity	Width	1070mm
	Depth	430mm max (475mm min (in corners only))
	Height	500mm
External Dimensions	Width	1255mm
	Depth	710mm
	Height	655mm
Total Weight	85.0kgs	
Maximum Ambient Temp.	35°C (95°F)	
Maximum Shelf Load	20kgs (per shelf)	
Set Temperature Accuracy	+/- 2°C	
Program Modes	8 Programs of 8 Segments	
Communication	Optional USB Module	
Material/Appearance	Grey Powdercoat / Galvanised Steel	
Transport Information	1200mm x 800mm Pallet (790mm High)	
Safety Features	Thermal Cut Out + Thermal Fuse	
Safety Standards	CE Marked, BS EN 61010-2-010	

easycomposites™
share the knowledge

Designed, manufactured and distributed by
Easy Composites Ltd

Easy Composites Ltd
Unit 39, Park Hall Business Village, Longton, Stoke on Trent, Staffordshire, ST3 5XA, United Kingdom.
Tel. +44 (0)1782 454499, Fax. +44 (01782) 596868, Email sales@easycomposites.co.uk, Web www.easycomposites.co.uk